Elucidating large-scale atmospheric controls on Bering Strait throughflow variability using a data-constrained ocean model and its adjoint

An T Nguyen[1,1], Rebecca A. Woodgate[2,2], and Patrick Heimbach[3,3]

[1]University of Texas-Austin
[2]University of Washington
[3]university of Texas at Austin

November 30, 2022

Abstract

A regional data-constrained coupled ocean-sea ice general circulation model and its adjoint are used to investigate mechanisms controlling the volume transport variability through Bering Strait during 2002 to 2013. Comprehensive time-resolved sensitivity maps of Bering Strait transport to atmospheric forcing can be accurately computed with the adjoint along the forward model trajectory to identify spatial and temporal scales most relevant to the strait's transport variability. The simulated Bering Strait transport anomaly is found to be controlled primarily by the wind stress on short time-scales of order 1 month. Spatial decomposition indicates that on monthly time-scales winds over the Bering and the combined Chukchi and East Siberian Seas are the most significant drivers. Continental shelf waves and coastally-trapped waves are suggested as the dominant mechanisms for propagating information from the far field to the strait. In years with transport extrema, eastward wind stress anomalies in the Arctic sector are found to be the dominant control, with correlation coefficient of 0.94. This implies that atmospheric variability over the Arctic plays a substantial role in determining Bering Strait flow variability. The near-linear response of the transport anomaly to wind stress allows for predictive skill at interannual time-scales, thus potentially enabling skillful prediction of changes at this important Pacific-Arctic gateway, provided that accurate measurements of surface winds in the Arctic can be obtained. The novelty of this work is the use of space and time-resolved adjoint-based sensitivity maps, which enable detailed dynamical, i.e. causal attribution of the impacts of different forcings.

1

Elucidating large-scale atmospheric controls on Bering Strait throughflow variability using a data-constrained ocean model and its adjoint

An T. Nguyen[1]*, Rebecca A. Woodgate[2], and Patrick Heimbach[1]

[1]University of Texas at Austin, Austin, TX, USA
[2]University of Washington, Seattle, WA, USA

Key Points:

- An adjoint sensitivity analysis is performed to quantify the role of atmospheric forcing on the variability of Bering Strait throughflow
- Primary driver of the variability is the wind stress over the Bering Sea and Arctic shelves, on timescales matching shelf wave propagation
- Impact of precipitation, although consistent with steric flow control, yield insignificant variability on monthly to interannual timescales

*Oden Institute for Computational Engineering and Sciences, The University of Texas at Austin, Austin, TX, USA

Corresponding author: An T. Nguyen, `atnguyen@oden.utexas.edu`

Abstract

A regional data-constrained coupled ocean-sea ice general circulation model and its adjoint are used to investigate mechanisms controlling the volume transport variability through Bering Strait during 2002 to 2013. Comprehensive time-resolved sensitivity maps of Bering Strait transport to atmospheric forcing can be accurately computed with the adjoint along the forward model trajectory to identify spatial and temporal scales most relevant to the strait's transport variability. The simulated Bering Strait transport anomaly is found to be controlled primarily by the wind stress on short time-scales of order 1 month. Spatial decomposition indicates that on monthly time-scales winds over the Bering and the combined Chukchi and East Siberian Seas are the most significant drivers. Continental shelf waves and coastally-trapped waves are suggested as the dominant mechanisms for propagating information from the far field to the strait. In years with transport extrema, eastward wind stress anomalies in the Arctic sector are found to be the dominant control, with correlation coefficient of 0.94. This implies that atmospheric variability over the Arctic plays a substantial role in determining Bering Strait flow variability. The near-linear response of the transport anomaly to wind stress allows for predictive skill at interannual time-scales, thus potentially enabling skillful prediction of changes at this important Pacific-Arctic gateway, provided that accurate measurements of surface winds in the Arctic can be obtained. The novelty of this work is the use of space and time-resolved adjoint-based sensitivity maps, which enable detailed dynamical, i.e. causal attribution of the impacts of different forcings.

Plain Language Summary

An ocean circulation model, that was adjusted to match observations, is used to investigate what are the important factors controlling the oceanic flow of water through the Bering Strait. Results show that the flow through the strait is related to surface atmospheric winds over the Bering Sea Shelf (south of the strait) and the near coastal regions of the Arctic Ocean (north of the strait). In the model, knowledge of these winds over the preceding 1 month allows us to reconstruct most of the changes in the flow through the strait. A somewhat surprising result is that winds in the Arctic have a greater influence on the amount of water flowing through the Bering Strait than winds over any region of the Pacific Ocean or the Bering Sea. The connection between the winds and the flow through the strait is strong enough that interannual changes in the winds may be used to predict interannual change in the flow. This predictive skill opens up the prospect for an improved understanding of the causes and mechanisms of flow changes at this important Pacific-Arctic gateway, provided that accurate measurements of surface winds over the Arctic can be obtained.

1 Introduction

The narrow ($\sim$85 km wide) and shallow ($\sim$50 m deep) Bering Strait is the only oceanic connection between the Pacific and the Arctic oceans (Fig. 1a). The annual mean flow is about 0.8 Sv (1 Sv = 10^6 m^3/s), northward through the strait, with a seasonal cycle ranging from $\sim$ 0.4 Sv to 1.4 Sv, and with significant interannual variability (Woodgate et al., 2005a, 2006, 2012). The Pacific waters carried by the flow (typically fresher than most Arctic waters, and seasonally warm and cold) contribute significantly to the stratification, as well as the heat, freshwater and nutrient budgets of the Chukchi Sea and the Arctic Ocean (e.g. Woodgate et al., 2005b; Serreze et al., 2006, 2007, 2016; Walsh et al., 1997; see Woodgate et al., 2015 and Woodgate, 2018 for reviews.) The Pacific Waters eventually exit the Arctic into the North Atlantic via the Fram Strait, Nares Strait, and the Canadian Arctic Archipelago, thus influencing the world ocean circulation (e.g. De Boer & Nof, 2004a, 2004b; Hu & Meehl, 2005; Hu et al., 2012; for a review, see Wadley & Bigg, 2002). Closer to the source, within the Chukchi Sea and possibly the western Arctic Ocean,

64 the inflow of warm Pacific waters is shown to influence sea-ice retreat (Woodgate et al.,
65 2010; Serreze et al., 2016). This in turn affects light availability in the water column on
66 the Chukchi Shelf, which, in combination with nutrient supply, may modulate regional
67 in-ice (Arrigo, 2014) and under-ice (Arrigo et al., 2012) ecosystem activity.

68   Given the influential role of the Bering Strait throughflow, and its potential soci-
69 etal impacts (e.g., driving changes important for Arctic residents, and industrialization,
70 such as resource exploitation and Arctic shipping/fishing), it is important to quantify
71 the properties of the flow and, where possible, understand the mechanisms controlling
72 how those properties change. Year-round in situ observations in the strait have been ob-
73 tained nearly continually since 1990 (see Woodgate et al., 2015 for a review) and have
74 indicated significant increases in volume ($\sim$ 0.6 to 1.1 Sv), heat and freshwater trans-
75 ports at least from the early 2000s to 2018 (Woodgate et al., 2015; Woodgate, 2018, Woodgate,
76 unpublished data). To date, however, the causes for these changes remain poorly under-
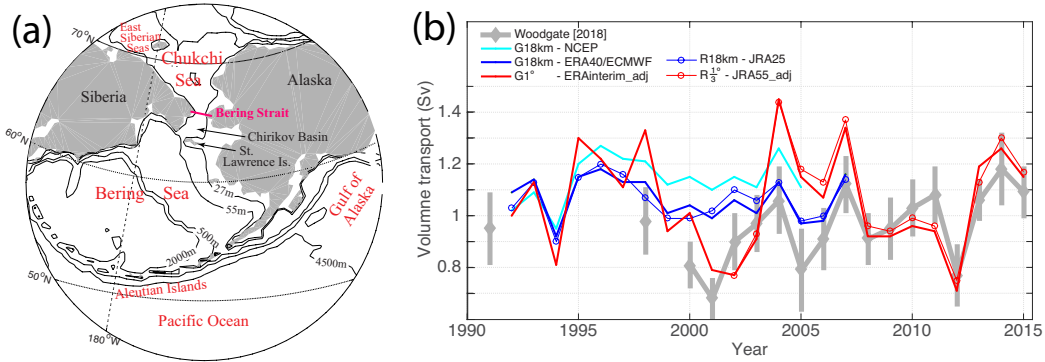77 stood.

Figure 1. (a) Geographic location of the Bering Strait, showing bathymetric contours from the global ECCO version 4 configuration. (b) Annual mean northward volume transport through Bering Strait, estimated from various sources: in situ moorings observations (including a standard correction for the Alaskan Coastal Current, thick grey, with error bars, Woodgate, 2018); global (G, thick color lines) and regional (R, thin color lines with symbol) ECCO configurations using various atmospheric reanalyses and model horizontal grid resolutions (given in legend). The atmospheric reanalyses are NCEP/NCAR (Kalnay et al., 1996), ERA-40/ECMWF (Uppala et al., 2005), JRA25 (Onogi et al., 2007), ERA-Interim (Dee et al., 2011), and JRA55 (Kobayashi et al., 2015). Simulations marked with extension "adj" are from adjoint-based optimization, where the atmospheric forcing fields have been adjusted within their respective uncertainties to bring the model into agreement with satellite and in situ observations, including Bering Strait mooring data (Forget et al., 2015; Fenty et al., 2015).

78   The flow through the Bering Strait is typically conjectured to be associated with
79 large scale oceanic "pressure head" forcing (usually cited as the difference in sea surface
80 height between the Pacific and the Arctic oceans), modified by local wind forcing within
81 the strait (see Woodgate et al., 2005b; Woodgate, 2018 for discussion). This hypothe-
82 sis was first discussed in the international literature by Coachman and Aagaard (1966),
83 a work which summarized prior Russian studies in the region, and, as other authors, tac-
84 itly assumed the pressure head forcing to be quasi constant in time. While the hourly
85 variability of the throughflow is extremely well correlated with the local wind (correla-
86 tion coefficient $\rho \sim 0.8$), longer term variability is not well explained by variations in
87 the local wind, leading to the suggestion that seasonal to interannual change relates to

88 variability in the pressure head drivings of the flow (Woodgate et al., 2010, 2012; Woodgate,
89 2018; Peralta-Ferriz & Woodgate, 2017).

90   The details of this pressure head forcing, however, have long remained unclear. The
91 origin of the pressure head itself has been suggested to be either steric (Stigebrandt, 1984;
92 Steele & Ermold, 2007) or driven by global winds (e.g. De Boer & Nof, 2004a, 2004b).
93 More recently, using a conceptual model, Danielson et al. (2014) correlated wind, pres-
94 sure, and sea surface height north and south of the strait with the throughflow and sug-
95 gested that the Bering shelf circulation is highly controlled by basin scale wind patterns,
96 particularly the Aleutian Low in the Bering Sea/Gulf of Alaska, with additional contri-
97 butions from the Beaufort and Siberian Highs and modifications from coastal shelf waves.
98 Kawai et al. (2018) also find relationships between model sea surface heights in the north-
99 east Bering Sea and the southwest Chukchi Sea with the flow through the Bering Strait.
100 Yet more recent work (Peralta-Ferriz & Woodgate, 2017) finds high correlations (cor-
101 relation coefficient $\rho \sim 0.6$) between monthly flow variability and a specific pattern of
102 ocean bottom pressure (OBP), viz a pattern dominated by low OBP in the East Siberian
103 Sea (assisted in winter by high OBP over the Bering Sea Shelf). Although that study
104 excludes interannual changes, it suggests a mechanism whereby westward Arctic coastal
105 winds invoke northward Ekman transport over the East Siberian Sea, enhancing the sea-
106 level difference between the Pacific and the Arctic and thus reducing sea level in the East
107 Siberian Sea and drawing flow northward through the strait. In contrast to prior work,
108 Peralta-Ferriz and Woodgate (2017) suggest the monthly variability of the flow to be pri-
109 marily driven by Arctic processes, not Bering Sea processes.

110   All of the above mentioned studies, however, are based on either simple theoret-
111 ical or statistical models. While these approaches may suggest possible connections, they
112 do not prove causality, nor do they expose underlying dynamical mechanisms. The com-
113 plexity of the system suggests that progress on understanding the large-scale mechanism
114 controlling throughflow variability may be made by drawing on the much more complete
115 numerical simulations of coupled sea ice-ocean general circulation models. In particu-
116 lar, we will utilize the non-linear inversion ("adjoint") framework established within the
117 global ECCO (Estimating the Circulation and Climate of the Ocean) version 4 coupled
118 ice-ocean configuration (Forget et al., 2015; Heimbach et al., 2019), which is based on
119 the Massachusetts Institute of Technology general circulation model (MITgcm, Marshall
120 et al., 1997; Adcroft et al., 2018) and its adjoint.

121   Unlike a perturbation simulation that quantifies the impact of the change of *one*
122 *input* on *all outputs* (directional derivative information), the adjoint model simulation
123 quantifies the sensitivity of *one output* to *all inputs* (gradient information). The adjoint
124 model provides a dynamical, i.e., causal link between the changed output quantity of in-
125 terest, such as the transport through the Bering Strait, and the inputs. Algorithmic dif-
126 ferentiation implements the adjoint, which formally represents the transpose of the lin-
127 earized model operator, on an elementary line-by-line basis using the chain and prod-
128 uct rules of differentiation. The transpose amounts to a time-reversal of information flow,
129 i.e., the resulting adjoint model propagates the change of one output back in time to as-
130 sess its sensitivity to changes in all inputs. With this framework, the flow of informa-
131 tion, e.g., sensitivity of the transport to the forcings, can be tracked from Bering Strait
132 back to its sources in space and time (Heimbach et al., 2010; Fukumori et al., 2015; Pil-
133 lar et al., 2016). Compared to purely statistical approaches (e.g., lag correlations or em-
134 pirical orthogonal function decomposition), the adjoint approach, being based on the nu-
135 merical model dynamics, provides a robust causal description. It elucidates mechanisms
136 driving the variability and allows for the assessment of time-lagged influences.

137   For this study, we considered several adjoint model configurations ranging from global
138 $1°$ to regional $1/3°$ resolution prior to choosing the ECCOv4 configuration. The narrow-
139 ness and shallowness of the Bering Strait suggest that a regional high resolution model
140 configuration would be more appropriate than a global and coarser resolution one. In

practice, however, we have consistently observed that, in the global MITgcm simulations (i.e., those which do not prescribe a set flow through the Bering Strait), a variety of model resolutions and wind forcing all produce similar, roughly 1 to 1.1 Sv annual mean northward flow through the Bering Strait (Fig. 1). While at smaller grid spacings the local circulation in the Bering and Chukchi Seas becomes more detailed, we do not encounter any systematic change in the total volume of the throughflow with increasing resolution. In addition, when a regional configuration (R) takes lateral boundary conditions from a global configuration, the Bering Strait transport is largely determined by the imposed lateral boundary conditions, irrespective of regional surface atmospheric forcing. This is evidenced in the similarity between the R1/3° run with JRA55 forcing (red line with symbol), which takes lateral boundary conditions from the global G1° run with ERA-Interim (red line) or R18km which used JRA-25 as forcing (blue line with symbol, Nguyen et al., 2011; Kinney et al., 2014), and the global run G18km from the ECCO2 project with ERA40 /ECMWF (blue line). Despite differences in atmospheric forcings, horizontal resolutions, treatment of dissipation and friction (ECCO2 models use Leith viscosity and free-slip boundary friction, ECCOv4r2 uses harmonic viscosity and no-slip boundary friction), and assimilation procedure (ECCO2 is restricted to a low-dimensional Green's functions based parameter calibration, ECCOv4r2 uses an adjoint-based state and parameter estimation approach), all models show low transports in 1994, 1999–2003, 2005, and high transports in 1995–1996, 2004, and 2007. All these reasons, in addition to computational efficiency, point to a global configuration at 1° as a sufficient choice for investigating large-scale controlling mechanisms for the Bering Strait transport variability in our study.

In general, the ensemble of model simulations, which use a variety of atmospheric forcings, encompasses the range of the observed transports, although there are differences in year-to-year variations and in long term trends, which show increasing flow in the observational data (Woodgate, 2018). For example, comparison between simulated and observed Bering Strait transport interannual trends show more consistency for the period 2008–2015 (simulated: 0.04 Sv/yr , observed: 0.03 Sv/yr, correlation coefficient: 0.9) than for the period 2004–2012 (simulated: -0.07 Sv/yr, observed: 0.01 Sv/yr, correlation coefficient: 0.2). The latter discrepancy between simulations and data is largely due to the anomalously high transport in 2004 and low transport in 2011, seen more extremely in the models than in the data. Nevertheless, we emphasize that the focus of this study is not on attempting to strictly reproduce the observed Bering Strait transport time-series over the decades. Instead, our goal is to deconstruct the time-series of the state estimate to identify the dominant regions, physical processes, and time-scales that control flow variability in the underlying dynamical model. Such information may then be used to understand possible causes of real world change and identify reasons for discrepancies between the models and the observations.

This paper is organized as follows. Section 2 describes the model configurations, the adjoint sensitivity experiments by which the sensitivity of the Bering Strait transport to various input atmospheric forcings are computed, and the procedure by which we then use these sensitivities to reconstruct the transport anomalies. Section 3 investigates the spatial and temporal patterns of the adjoint sensitivities and quantifies the contributions of atmospheric forcings at various time-scales (interannual, seasonal, and sub-monthly) to the Bering Strait transport. Section 4 discusses the regions found to be most influential on the variability of the throughflow and the underlying physical mechanisms. In addition, it considers the role of precipitation as the steric driving mechanism of the Bering Strait transport variability. The transport extrema between 2004–2007 seen in the model are also discussed. Section 5 summarizes the key findings.

2 Methodology

2.1 Model description

The ECCO version4 release 2 (ECCOv4r2) global ocean-sea ice state estimate at nominally 1 degree horizontal resolution (Forget et al., 2015; Fukumori et al., 2018) is the primary modeling tool in this study. The term "state estimate" here refers to the result of a data assimilation procedure by which a general circulation model is fit, in a least-squares sense, to a wide range of observations. The observational constraints used for the assimilation in ECCOv4r2 include as many ocean and sea ice observations as available and practical, including satellite sea surface heights and temperature, sea ice concentration from Special Sensor Microwave/Imagers (SSM/I, Cavalieri et al., 1991), Argo floats (Roemmich et al., 2009), Ice Tethered Profilers (Toole et al., 2006), and moorings at important Arctic and Nordic Seas gateways (see Forget et al., 2015 for a complete list). Note that Bering Strait mooring data have been included as a constraint. Unlike in "reanalyses", the assimilation procedure is such that the underlying conservation laws as expressed by the governing equations for momentum and tracers are strictly enforced, thus enabling accurate analyses of budgets and causal mechanisms (Stammer et al., 2016; Wunsch & Heimbach, 2007, 2013).

We summarize here only the salient features of the configuration that are relevant for our investigation. A more thorough description of ECCOv4r2 can be found in Forget et al. (2015) and Fukumori et al. (2018). The full period of ECCOv4r2 is 1992–2013. The choice of length of an adjoint sensitivity run within this period does not need to match that of ECCOv4r2. Instead it is guided by the time-scales of interest of the physical processes being studied. For this work we choose a shorter period of 01/Jan/2002–31/Dec/2013 to allow us to look at sensitivity **at lag time** varying from 1 hour to 12 years. Our results show that this length of study is likely sufficient, as our dynamical reconstruction recovers a high fraction of explained variance observed by timescales much shorter than 12 years. The initial conditions for our study come from the ocean and sea ice state of ECCOv4r2 on 01/Jan/2002. The surface atmospheric forcing come from the ECCOv4r2 adjusted ERA-Interim fields for 2002–2013, as described in Forget et al. (2015). The model is also forced with monthly-mean estuarine runoff, which are based on the Regional, Electronic, Hydrographic Data Network for the Arctic Region (R-ArcticNET) dataset (Lammers & Shiklomanov, 2001; Shiklomanov et al., 2006).

The grid spacing at the Bering Strait is ∼48 km in the horizontal and 10 m in the vertical. Although this gives only two grid points across the Bering Strait, as shown in Fig. 1b, the total transport at the strait is very similar to that in the high resolution models. The model uses a non-energy-conserving semi-implicit time-stepping algorithm to solve for the free surface elevation (Marshall et al., 1997) in rescaled z^* coordinates (Adcroft & Campin, 2004) with a non-linear free surface capability and real freshwater flux boundary condition (Campin et al., 2004).

Prior studies show that this semi-implicit method can damp gravity wave amplitudes by up to 50% and reduce phase speeds by up to 35% within one cycle (Kurihara, 1965; Casulli & Cattani, 1994; Campin et al., 2004). In addition, wavelengths and phase speeds can be further modified for unresolved baroclinic shelf and coastally trapped Kelvin waves in coarse grid resolution models with added friction (Hsieh et al., 1983; Griffiths, 2013), especially when the model coastline is not aligned with the C-grid orientation (Schwab & Beletsky, 1998; Griffiths, 2013). For ECCOv4r2, the use of partial cells to represent topography (Adcroft et al., 1997) alleviates some of the grid-resolution related problems. However, in combination with added horizontal and vertical friction, the model's representation of theoretical Kelvin and coastal shelf waves are modified numerical equivalents and should be interpreted with caution. This applies to "reverse Kelvin wave" propagation in the adjoint model as much as it applies to the full nonlinear forward model.

242 As such the adjoint model exposes these adjustment processes and may help to uncover
243 how adjustment to external forcing is conveyed in the model being studied.

244   The configuration used in this study utilizes the adjoint capability developed within
245 the ECCO consortium (Wunsch & Heimbach, 2007, 2013) but with several approxima-
246 tions described in Forget et al. (2015). The coupled ocean-sea ice adjoint model has been
247 generated by means of algorithmic differentiation (Heimbach et al., 2010; Fenty & He-
248 imbach, 2013). Model-data misfits are reduced systematically through gradient-based
249 iterative minimization of a least-squares misfit function (adjoint or Lagrange Multiplier
250 method) by adjusting model parameters and input fields (together termed "control vari-
251 ables"), which carry sizable uncertainties (Forget et al., 2015; Stammer, 2005; Fenty &
252 Heimbach, 2013).

253   As described in Forget et al. (2015), for ECCOv4r2, the linearization of the sea ice
254 model and the mixed-layer parameterization represented in the adjoint model contains
255 several approximations. One way to assess the impact of these simplifications in the ad-
256 joint model is to quantify how well a propagating perturbation that is simulated with
257 the full nonlinear forward model can be reconstructed from the adjoint gradients with
258 the reduced physics in a Taylor series expansion. As shown in Section 3, the reconstructed
259 time-series of transport anomalies based on the linearized (and approximated) adjoint
260 sensitivity can capture very well the transport anomalies obtained from forward model
261 that used the full physics. This indicates that the impact of these reduced linearized physics
262 in the adjoint model is small for the Bering Strait transport problem.

263   For the current study, similar to ECCOv4r2, the control variable space Ω is com-
264 prised of the two components of the surface momentum fluxes, 10-m east- and north-ward
265 wind stresses, as well as five surface atmospheric variables: precipitation, downward short-
266 and long-wave radiation, surface specific humidity, and 10-m air temperature. Uncer-
267 tainties for these control variables are described in Fenty and Heimbach (2013) and Chaudhuri
268 et al. (2013, 2014). Although runoff and evaporation are not part of the control space,
269 in practice they project onto the precipitation sensitivities, interpreted as linear com-
270 bination of net freshwater fluxes.

2.2 Adjoint sensitivity and reconstruction

272   The forward and adjoint models can be used to assess how variability in the sur-
273 face atmospheric forcings influence the flow through the Bering Strait by the following
274 procedure. The model is first integrated forward in time from 2002–2013. The mean Bering
275 Strait volume transport at a time t, $J(t)$ over a period T starting from any given time
276 $t - T/2$ is defined as:

$$J(t) \equiv \frac{1}{T} \int_{t-T/2}^{t+T/2} \int_A \mathbf{u}(t') \cdot \hat{\mathbf{n}} \, dA \, dt' \tag{1}$$

278 where $\mathbf{u}$ is the time-varying 2-D horizontal velocity vector field on a vertical section across
279 the strait, and A is the cross-sectional area of the strait whose normal component is $\hat{\mathbf{n}}$.
280 The anomaly δJ is defined as $J(t)$ minus the time-mean, $\overline{J_{2002-2013}}$, of our integration
281 period of 2002–2013:

$$\delta J(t) \equiv J(t) - \overline{J_{2002-2013}} \tag{2}$$

283 The adjoint model computes sensitivities $\partial J/\partial \Omega$ of J to all control variables that are part
284 of the control vector Ω. In the following we will interchangeably refer to these $\partial J/\partial \Omega$
285 as "sensitivities", "gradients", "influences", and "partial derivatives" as, dependent on
286 the context, sometimes one term conveys the point in the discussion more clearly than
287 the others. The gradients can be efficiently computed for a very high-dimensional con-

trol space via the adjoint method (Wunsch & Heimbach, 2007, 2013), i.e. one adjoint integration yields all partial derivatives $\partial J/\partial \Omega_k$ simultaneously for each of the individual surface atmospheric forcing variables Ω_k. The gradients consist of two-dimensional surface fields (in x_1, x_2) and these derivatives are updated at regular (e.g., bi-weekly) intervals (linearly interpolated in between) along the model temporal trajectory. Their spatial and temporal patterns can be used to reconstruct (in the sense of a Taylor series expansion) the forward time-series of the throughflow **anomalies** $\widetilde{\delta J}(t)$ as follows (Fukumori et al., 2015; Pillar et al., 2016),

$$\widetilde{\delta J}(t) = \sum_k \widetilde{\delta J_k}(t) = \sum_k \int_{t_0}^{t} \int_{x_1} \int_{x_2} \frac{\partial J}{\partial \Omega_k}(x_1, x_2, \alpha - t)\, \delta\Omega_k(x_1, x_2, \alpha) dx_1 dx_2 d\alpha \quad (3)$$

where $\widetilde{\delta J}(t)$ is the reconstructed transport anomaly, with the $\sim$ symbol added to distinguish it from the anomaly obtained from the forward run δJ_{fwd}. $t_0 = 01/\text{Jan}/2002$ is the time when the model integration starts, α is a time prior to the current time t, with values thus ranging from t_0 to t, $(\alpha - t)$ is the time-lag, $\delta\Omega_k$ the atmospheric forcing anomalies associated with the forcing field k, and $\partial J/\partial \Omega_k(x_1, x_2, \alpha-t)$ gives the influence on δJ of variable $\delta\Omega_k$ at lag time $\alpha - t$ and spatial location $[x_1, x_2]$.

For each k, the anomalies $\delta\Omega_k$ are computed as the input forcings minus their respective 2002–2013 mean, $\delta\Omega_k(t) = \Omega_k(t) - \overline{\Omega_{2002-2013}}$. The peak-to-peak ranges of $\delta\Omega_k$ come primarily from the seasonal cycles, with 90-percentile values of 0.15 N/m^2, 0.12 N/m^2, 17°C, 0.006 kg/kg, 185 W/m^2, 87 W/m^2, and 8×10^{-8} m/s for zonal and meridional wind stresses, 2 m air temperature, specific humidity, downward short- and long-wave radiation, and precipitation, respectively.

Eqn. (3) indicates that the anomaly $\widetilde{\delta J}(t)$ at any time t is a convolution of the time-lagged $(\alpha-t)$ gradient $\partial J/\partial \Omega$ with the forcing anomaly $\delta\Omega$ at time α. In simpler language the equation states that the reconstructed anomaly $\widetilde{\delta J}(t)$ is computed from the sum of point-wise influences (in space and time) integrated over the time α, which ranges from t_0 to the time t of consideration. To put this more simply still, the adjoint technique quantifies the influence of a forcing at a point in space on a quantity of interest (here the Bering Strait transport) through anomaly propagation (usually in the form of oceanic linear adjustment processes) at various time lags (here up to the length of our model simulation, 12 years). This implies that contributions to the transport anomaly $\delta J(t)$ at any time t will depend on how sensitive $\delta J(t)$ is to each forcing anomaly $\delta\Omega_k$ at various time-lags corresponding to prior days, months or years, and the spatial distribution of the sensitivity locally and away from the strait. Note that the time-lag $(\alpha-t)$ only takes on negative values, indicating that a past event has influence on a future δJ. If the system is sufficiently linear, the reconstructed $\widetilde{\delta J}(t)$ will be close to the full $\delta J_{fwd}(t)$ obtained with the full nonlinear forward model.

Although in theory, being the derivative of a nonlinear operator, $\partial J/\partial \Omega$ may vary with the time when J is defined, a reasonable approximation is to assume that if there is a dominant linear mechanism linking the drivers $\delta\Omega$ with δJ, then $\partial J/\partial \Omega$ should be, to first order, independent of the time when J is defined. Tests (see Supplemental Material) show this to be the case, and thus in what follows, we use $\partial J/\partial \Omega$ that correspond to a J defined as the monthly mean Sept 2013 transports. This choice of $J_{Sep/2013}$ is based on the consideration that the September transports lie between the seasonal transport extrema (Woodgate et al., 2005a) with maximum δJ during the summer months and minimum δJ during the winter months. With J defined as $J_{Sep/2013}$, we compute time-lagged gradients $\partial J/\partial \Omega$ at discrete, monthly intervals.

We will denote $\frac{\partial J}{\partial \Omega(l)}$, where $l = \{1, 2, \ldots\}$ months, as the monthly mean sensitivity spanning the time range $[l-1, l)$ months, and refer to this quantity as l-month
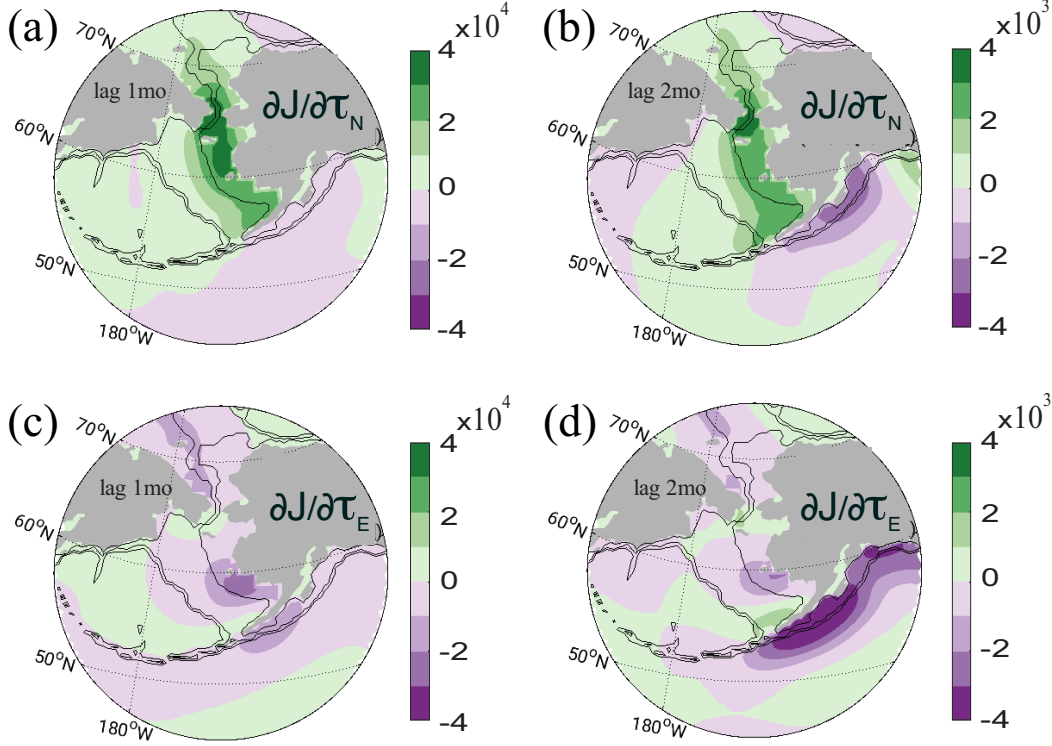
Figure 2. Sensitivity of Bering Strait volume transport anomalies to increments in (a–b) northward wind stress $\frac{\partial J}{\partial \tau_N}$ and (c–d) eastward wind stress $\frac{\partial J}{\partial \tau_E}$ in units of $(m^3/s)/(N/m^2)$ at (a,c) 1-month and (b,d) 2-month lags (see Section 2.2 and eqn (3) for the definition of lag.) A positive gradient here implies that a positive increment $\delta\tau_{E,N}$ will result in a positive increase in the $\widetilde{\delta J}$ with magnitude as indicated in the color scales and units. The highest sensitivity of order 10^4 $(m^3/s)/(N/m^2)$ is found for $\frac{\partial J}{\partial \Omega(1)}$, i.e., within the 1-month lag. It is highly localized to the Bering Strait and shallow Bering and Chukchi Sea shelves. Bathymetric contours are the same as shown in Fig 1a.

lag sensitivity. For example, the 1-month lag sensitivity, $\frac{\partial J}{\partial \Omega(1)}$, is the time average over all sensitivities from lag zero to lag 1 month. These monthly mean sensitivities are 2D surface fields.

3 Results

3.1 Adjoint sensitivity maps

Monthly average adjoint sensitivities were computed for all seven atmospheric control variables at different monthly-averaged lag times. The largest influence found was related to surface wind stress. Sensitivities with respect to meridional (N) and zonal (E) wind stress $\frac{\partial J}{\partial \tau_N}$ and $\frac{\partial J}{\partial \tau_E}$ are highest at 1-month lag, and both wind stress components contribute significantly to $\delta J(t)$ (Fig. 2).

The largest sensitivities are found in the strait itself, with $\frac{\partial J}{\partial \tau_N}$ being approximately (in magnitude) two times larger than $\frac{\partial J}{\partial \tau_E}$. This is consistent with previous observation-based results that the northward flow through the strait is best correlated with the wind at heading 330° (Woodgate et al., 2005b). Away from the strait, the largest sensitivi-

ties are found over the shallow shelves south and north of the strait, especially the Bering Sea Shelf above 500 m (for northward wind stress), the Gulf of Alaska, the Chukchi Sea, and the East Siberian Sea shelf break. Within these regions, over the northern Bering Sea Shelf between 0–150 km south of the strait, τ_N has the strongest impact on the strait transport at up to 1-month lag, with positive wind change over the Bering Sea Shelf resulting in positive increase in Bering Strait transport (see the range in the color-scale in Fig. 2a). The combination of positive $\partial J/\partial \tau_N$ and negative $\partial J/\partial \tau_E$ parallel to and between the Alaskan coast and the 500 m isobath in the Bering Sea implies that northwestward wind stress here promotes positive δJ, likely via a mechanism of onshelf transport.

Away from the strait, there exist several regions with significant influences as well. In particular, southeast of the Aleutian islands, negative $\partial J/\partial \tau_N$ and $\partial J/\partial \tau_E$ along the Alaskan coast and the Aleutian Islands suggest that southwestward wind stress in this region promotes the strengthening of the Alaska Coastal Current (Weingartner et al., 2005), leading to enhanced northward flow through the Aleutian Islands onto the Bering Shelf and also increasing δJ at the Bering Strait at lags of 1–2 months. These results are consistent with statistical wind-to-transport correlations of Danielson et al. (2014).

Inside the Arctic, positive $\partial J/\partial \tau_N$ and negative $\partial J/\partial \tau_E$ indicate northwestward wind stress anomalies in the Chukchi and East Siberian Seas promote δJ increases. The likely mechanisms are those suggested by Peralta-Ferriz and Woodgate (2017), who find significant correlations between westward winds along the East Siberian Sea shelf break and the flow through the Bering Strait, especially with the component of the flow not associated with the local wind (i.e., the pressure head term, Woodgate, 2018). Peralta-Ferriz and Woodgate (2017) propose a mechanism by which these westward winds in the Arctic move waters off the East Siberian Sea shelf via Ekman processes, lowering sea level in the East Siberian Sea, and generating a pressure gradient that enhances northward flow of waters through the strait (as per the theory of flow through a rotating channel, see e.g., Toulany & Garrett, 1984). These regions (both south and north of the strait) are suggested areas of formation of shelf waves that may contribute to driving Bering Strait transport anomalies (Danielson et al., 2014). Section 4 discusses in more detail shelf waves as a mechanism for propagation of sensitivities to the Bering Strait.

At a 2-month time lag, sensitivities drop approximately one order of magnitude, and are spread further north and south of the strait (Fig. 2b,d). All patterns and signs of $\partial J/\partial \tau_{E,N}$ remain consistent with those within the 1-month lag. Additional features include those further south along the western Canadian coast, where an increase in northwestward wind stress promotes a positive δJ at the strait two months later. Within the Arctic, southwestward wind stress anomalies in the Kara Sea and much further away in the eastern Nordic Sea (both not shown) also appear to have some influence on the Bering Strait throughflow, although the magnitudes of sensitivity is significantly reduced such that their overall contribution to δJ is negligible (see further discussion in Section 3.4).

After two months, the sensitivities decrease by another factor of 5–10, such that their contribution to the transports is insignificant (not shown).

3.2 Reconstruction of transport anomaly time series

To investigate the main driver of the throughflow variability at Bering Strait in the model, we reconstruct the transport anomaly time series by summing the contributions from $\partial J/\partial \Omega$ globally, following eqn. (3). Fig. 3 shows δJ_{fwd} obtained from the model forward run (black) and $\widetilde{\delta J}$ from the reconstruction via eqn. (3) (red, blue). Two reconstructions were made, one using only contributions from the northward and eastward wind stress anomalies (blue in Fig. 3) for the purpose of isolating the role of winds, and one using contributions from all seven atmospheric forcing fields (red) for the purpose of assessing the role of the non-wind stress terms. Also shown are the correlation coefficient
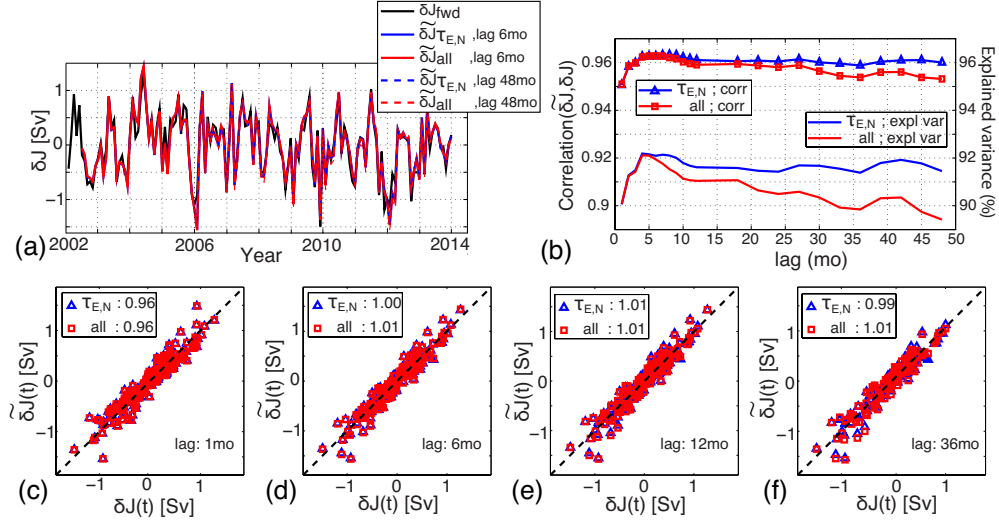
Figure 3. (a) Time series of $\widetilde{\delta J}(t)$ reconstructed using anomalies of either only wind stress (blue) or all seven atmospheric components of Ω (red), to be compared with the forward time series $\delta J_{fwd}(t)$ in black. (b) Correlation coefficient ρ between $\widetilde{\delta J}$ (the reconstructed transport anomalies) and δJ_{fwd} (the transport anomalies from the forward model; lines with symbols), along with percentage of explained variance (PEV, line without symbols, using y-axis to the right) for reconstructions which are cumulatively summed over the range of lags indicated in the abscissa. See Section 3.3 for discussion on the degradation of ρ and PEV when all atmospheric forcing terms are used in the reconstruction. (c–f) Scatter plots of the the forward δJ_{fwd} with full model dynamics versus the reconstructed time series $\widetilde{\delta J}$ for lags of up to (c) 1 month , (d) 6 months, (e) 12 months, and (f) 36 months. Numbers in the legend indicate the slope of the fitted line, with the one-to-one line shown in dashed black for reference.

ρ and percentage of explained variance (PEV) between the forward and reconstructed time series. The contribution from the wind components (blue curve in Fig. 3a) is almost identical to (and thus on the plot almost completely overwritten by) the contribution from all components (red curve) indicating that the non-wind components have a very small effect.

The reconstructed time series $\widetilde{\delta J}_{all}$ (red) correlates strongly ($\rho > 0.94$) with the forward model time series δJ_{fwd} (black) at all time lags (Fig. 3c–f), with slopes in the scatter plots of $\widetilde{\delta J}_{all}$ versus δJ_{fwd} ranging between 0.96 and 1.01. This suggests that the reconstruction captures nearly the full dynamics of the strait transport anomalies simulated with the forward model. The reconstruction using only the 1 month lag contribution still captures $\sim$90% of the variability and 96% of the magnitude (slope on scatter plot). The wind stress components are the dominant contributors to the transport anomalies at monthly to multi-year time-scales, with all other atmospheric forcing terms contributing only $\sim$1–2% (compare the slope of "all" versus $\tau_{E,N}$ in Fig. 3c-f).

A noticeable degradation of ρ and PEV when including contributions from longer time lags can be seen when all forcing terms are included (Fig. 3b). A breakdown of contributions from individual forcing terms shows that the terms associated with heat fluxes (e.g., air temperature, downward long and short waves) contribute approximately equally to the degradation (not shown). We speculate that these terms may have an accumulated non-linear effect on the water column with time that the adjoint sensitivities cannot fully capture due to some of the simplified physics in the adjoint model, as discussed
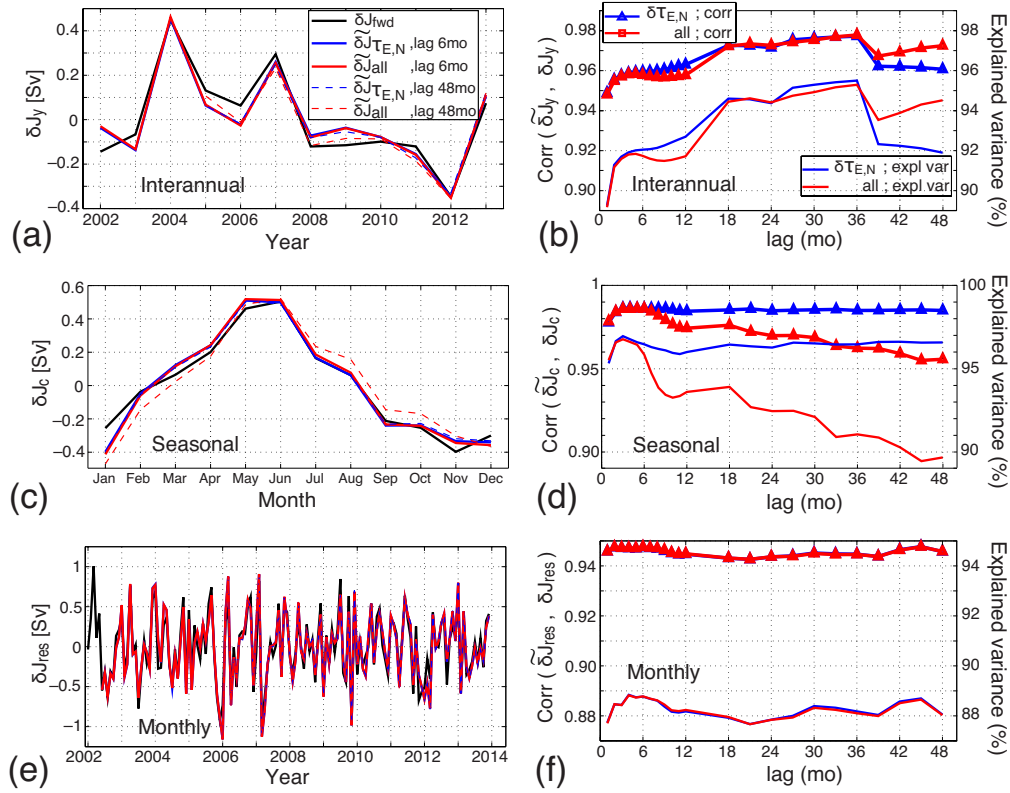
Figure 4. Decomposition of the forward model $\delta J_{fwd}(t)$ and reconstructed $\widetilde{\delta J}(t)$ into their annual mean (a), 12-mo climatology (or seasonal, c), and monthly (or high-frequency, e). Left panels (a,c,e) show the time series of each component, while right panels (b,d,f) show correlation ρ and percentage of explained variance (PEV) between the reconstructed $\widetilde{\delta J}$ and the model forward δJ_{fwd} time series for annual (b), seasonal (d) and monthly (f). See text for discussion on the degradation of ρ and PEV when all atmospheric contribution terms are included in the reconstruction of the climatological time series in (d).

in Section 2. As a result, errors in $\widetilde{\delta J}$ are aggregated with increasing cumulative lags the further back in time the reconstruction is carried out. This degradation in the reconstruction due to contributions from buoyancy terms remains insignificant after 36 months, with correlation coefficients and explained variance still above 0.95 and 0.9 (Fig. 3b). It has also been observed in previous adjoint-based reconstructions (see Pillar et al., 2016; Smith & Heimbach, 2018), but a full investigation of whether the degradation is due to inaccuracies in the approximated adjoint model or missing physics in the forward model is beyond the scope of this study. Excluding the contributions from air temperature and downward radiation, the correlation between the $\widetilde{\delta J}$ reconstructed using wind stress and δJ_{fwd} remain steady when longer time lags are considered, suggesting that there is a close correspondence between the wind stress and the Bering Strait transport anomalies, and that the effect of winds has a short time history (Fig. 3f). Finally, adding the contribution from precipitation to $\widetilde{\delta J}$ (not shown) did not change the correlation significantly.

3.3 Decomposing $\widetilde{\delta J}(t)$ into temporal components

To examine short-to-long time-scale contributions, the time series of monthly transport anomaly from both the forward model δJ_{fwd} and the adjoint-based reconstruction

438 $\widetilde{\delta J}(t)$ can alternatively be decomposed into its monthly (sub-seasonally), seasonally (12-
439 month climatology), and multi-year components (Fig. 4). We calculate this discretely,
440 rather than as a spectral decomposition as our time series is comparatively short. For
441 any time series of anomalies, the decomposition is done as follows. The 2002–2013 an-
442 nual mean time series (12 annual means), denoted by subscript "y", is obtained by com-
443 puting the average of the anomaly for each calendar year. The monthly climatology time
444 series (12 monthly means), denoted by subscript "c", is computed by subtracting from
445 each monthly value the annual average for that year, and then averaging over each month
446 for the entirety of the record. Finally, the "residual", denoted by subscript "res", is com-
447 puted by subtracting from each monthly anomaly both the annual mean and the sea-
448 sonal climatology for that month. The decomposition described above operates strictly
449 on the transport anomaly time-series δJ_{fwd} or $\widetilde{\delta J}$. Note that $\widetilde{\delta J}$ is obtained from eqn. (3)
450 using the total (i.e., non-decomposed) forcing anomalies $\delta\Omega$.

451 Given the dominance of wind stress forcing on δJ at short lags (Section 3.2), we
452 explore a second approach for the temporal decomposition that would allow us to relate
453 directly the temporally decomposed forcings $\delta\Omega_{[y,c,res]}$ to the decomposed $\widetilde{\delta J}_{[y,c,res]}$ as
454 follows:

455
$$\widetilde{\delta J}_{[y,c,res]}(t) \quad \approx \quad \int_{t_0}^{t} \int_{x_1} \int_{x_2} \frac{\partial J}{\partial \Omega_k}(x_1, x_2, \alpha - t)\ \delta\Omega_{[y,c,res],k}(x_1, x_2, \alpha)\ dx_1\ dx_2\ d\alpha \quad (4)$$

456 A comparison of these two approaches (i.e., a decomposition obtained from the full
457 reconstructed $\widetilde{\delta J}$ and that obtained from approximation following eqn. 4) can be found
458 in the Supplemental Material. It shows that both methods yield approximately the same
459 results. The important advantage of performing the reconstruction following the approx-
460 imate method of eqn. (4) is that it is then straightforward to calculate, for example, the
461 interannual transport anomalies, $\widetilde{\delta J}_y$, from the interannual forcing anomalies, $\delta\Omega_y$, of
462 any forcing reanalysis. In the following, all reconstructed decompositions were obtained
463 using eqn. (4).

464 Results of the reconstructed $\widetilde{\delta J}_{[y,c,res]}$ as well as comparisons of these time-filtered
465 components to their counterparts from the forward model are shown in Fig. 4. The re-
466 constructed time series based on annual-means, $\widetilde{\delta J}_y$ (Fig. 4a-b), capture well the sim-
467 ulated decadal change seen in $\delta J_{fwd,y}$. It has an apparent maximum ρ and PEV when
468 summing in time up to a lag of 36-months, but note that the change in correlation and
469 PEV is very small (0.01 and 1%). There appears to be a small annual cycle (at every
470 incremental 12-month lag) in both ρ and PEV, with a noticeable drop-off after 36-month
471 (Fig. 4b). One possible cause might be that 36-months is the time-scale where linear-
472 ity assumption holds and that beyond 36-months this assumption begins to break down.
473 Overall the correlation and PEV remain very high, nevertheless ($\rho > 95\%$ and $PEV >$
474 92%).

475 There is a very small difference of 1–2% between using only wind stress and using
476 all atmospheric forcing variables for the reconstruction, implying that to first order winds
477 are the controlling factor, even at the multi-year time-scale, in setting the annual mean
478 anomalies (above the long-term mean flow of ~ 1 Sv). For short lags the local winds dom-
479 inate, but for longer lags the net effect of winds is spread out over a much larger (basin-
480 scale) region, and we will return to this in Section 3.4.

481 The reconstructed time series based on monthly climatological values, $\widetilde{\delta J}_c$ (Fig. 4c-
482 d), exhibit a pronounced degradation of ρ and PEV when using all atmospheric variables
483 (red line) after ~ 6 month lag. An inspection of the reconstructed seasonal cycle of the
484 transport anomalies (Fig. 4c) shows that as more lagged sensitivities are used for the re-
485 construction, there is a noticeable shift in timing in the entire seasonal cycle, e.g., later

increase, later maximum, later decrease. As in the previous section, we speculate that this degradation is due to non-linear effects of longwave and shortwave absorption in the ocean, such that beyond ∼5 months the linearity assumption for buoyancy flux sensitivities breaks down. What remains robust is that the sensitivity patterns from the first two months (Fig. 2) capture $> 98\%$ of the correlation and $\sim 97\%$ of PEV. Even after a 48 month lag, despite the degradation the PEV is still $\leq 90\%$. Overall, the reconstruction using only winds yields the highest correlation and PEV.

The remaining Bering Strait transport residual at sub-seasonal (monthly) time-scale, δJ_{res}, is still well reconstructed (88% of PEV) by the local wind within four months prior, with minimal improvement ($\sim 1\%$) after the first month lag (Fig. 4f).

Overall, the time-filtered reconstructions reveal that adjoint sensitivity $\partial J / \partial \Omega$ for wind stress captures 95–98% of the variability of the full time series of the Bering Strait transport anomaly at monthly to multi-year time-scales (Fig 4b,d,f). The degradation in correlation between $\widetilde{\delta J}$ and δJ_{fwd} (Fig. 3b) is largely due to degradation in the reconstructed seasonal cycle (Fig 4d). Despite the degradation, the correlation remains high, with ∼90% of the variance captured at the seasonal time-scale. As the difference in the reconstruction using all forcings and using only wind stresses is small, for the remainder of the analyses we will focus on reconstructions using only wind stress.

3.4 Decomposing $\widetilde{\delta J}(t)$ in space

Up to now, the reconstruction of $\widetilde{\delta J}$ has been performed by integrating the effect of winds over the entire globe (see eqn. 3). However, as discussed in Section 3.1, regions near the strait and further away can contribute coherently or non-coherently at different time lags. Fig. 5a shows a breakdown of contributions for the three most important regions, which are chosen heuristically to include what our analysis shows are the major regions of influence: (1) the Bering Sea Shelf (BeS), situated south of the strait with dominantly positive sensitivity to northward wind stress; (2) the Gulf of Alaska (GoA), situated further south of the strait with dominantly negative sensitivity to northward wind stress; and (3) the Chukchi and East Siberian Seas (Ck+ESS) situated north of the strait with positive sensitivity to northward wind stress.

The convolution restricted to these individual regions (Fig 5b) can be compared with a global convolution (blue curve in Fig. 3 and Fig. 4). Only a limited period (2003–2007) of the full time series (2002–2013) is presented here to simplify the visualization of the regional contribution in individual years. With a few exceptions, regions BeS and Ck+ESS contribute approximately equally in sign and magnitude to the total month-to-month variation (each ∼40%). Region GoA contributes very little (∼4%) to the total, and is therefore omitted from Fig. 5b for clarity. The dominance of the combined BeS and Ck+ESS regions can be seen clearly in the scatter plots (Fig. 5c-d) for lags of up to 12-months. Specifically, the green line (the sum of the BeS and Ck+ESS components) is close to the grey lines, indicating that other terms are small. Summing contributions up to 12-months lag does not significantly improve the reconstruction (i.e., compare BeS plus Ck+ESS 1-month lag correlation of 0.91 with BeS plus Ck+ESS 12-month lag correlation of 0.91).

Next, a more comprehensive spatial decomposition of the reconstruction is performed to investigate the role of local versus far field influences in modifying the seasonal and interannual variability. Seven regions were identified based on the magnitude of the adjoint sensitivity in both wind stress components (Fig. 6). Results show that all the regions with significant influence are either over shallow high latitude shelves or along the coastlines, and all are "upstream" of the Bering Strait in a Kelvin wave-propagation sense. In the northern hemisphere, the coastally trapped Kelvin wave propagates with the coast on its right, and thus the Bering Sea Shelf and the East Siberian Sea are both upstream of the Bering Strait, and the Pacific Russian coast and the Arctic Alaskan Coast are both
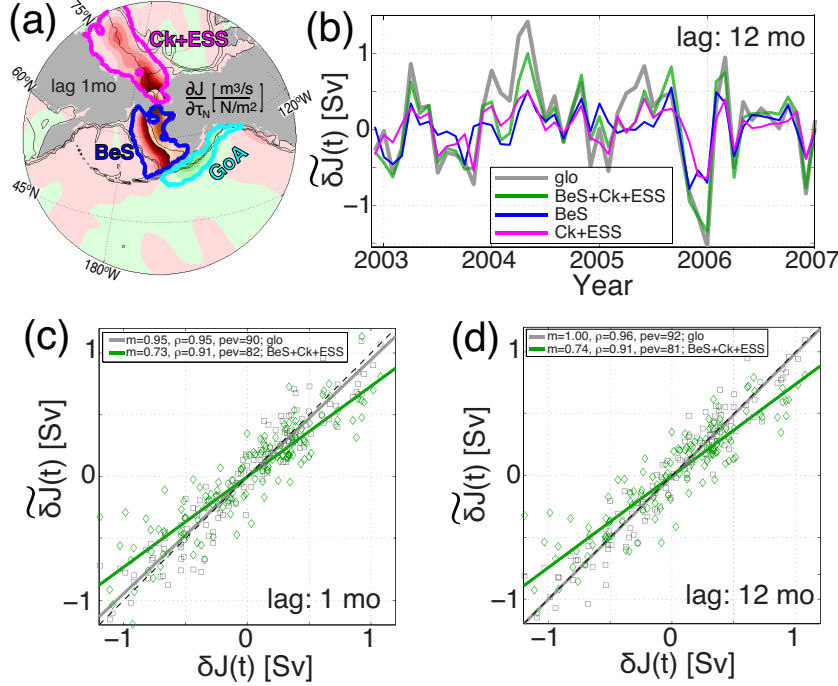
Figure 5. (a) Three regions that contribute the most to the Bering Strait transport anomalies at 1 month time lag: the Bering Sea Shelf (BeS), Gulf of Alaska (GoA), and the Chukchi and East Siberian Seas (Ck+ESS). (b) Reconstruction, using winds only, as a function of region of influence, including some combinations of regions (colors as per key) and the global sum (glo, grey line) for comparison. Scatter plot of the reconstructed $\widetilde{\delta J}$ and forward δJ_{fwd} summed to lags of (c) 1-month and (d) 12-months. Legends in (c–d) show the fitted slope (m), correlation (ρ), and percentage of explained variance (PEV).

downstream of the strait in the Kelvin wave-propagation sense. The rest of the ocean interior, labeled "rest", generally has a smaller contribution than any of the seven identified regions. A hypothesis for the mechanisms that determine these regions will be presented in Section 4.

In the reconstruction of the seasonal cycle (Fig. 6b), while the Bering Sea and the combined Chukchi and East Siberian Seas still give the largest contributions (each ∼35%), it is interesting to note the significant contributions (∼ 30%) of regions further north of the strait such as the Laptev Sea (La), the Barents Sea (Ba), and the eastern North Atlantic (Atl).

In the reconstruction of the interannual time-series (Fig. 6c), the Bering Sea and the combined Chukchi and East Siberian Seas dominate most of the time, though occasionally with opposite signs. Contributions from the Bering Sea Shelf are highly variable in sign. Due to competition with other regions, they do not alone determine the sign of the annual-mean anomaly. Overall, the Pacific-sector contributions to Bering Strait transport originating from the Northwest Pacific (Pa) and Gulf of Alaska (GoA) are small, (∼3%) except for the years 2005 and 2011 when they are large enough to offset the contribution from the Bering Sea Shelf and result in a change of sign of the simulated annual mean transport anomaly.
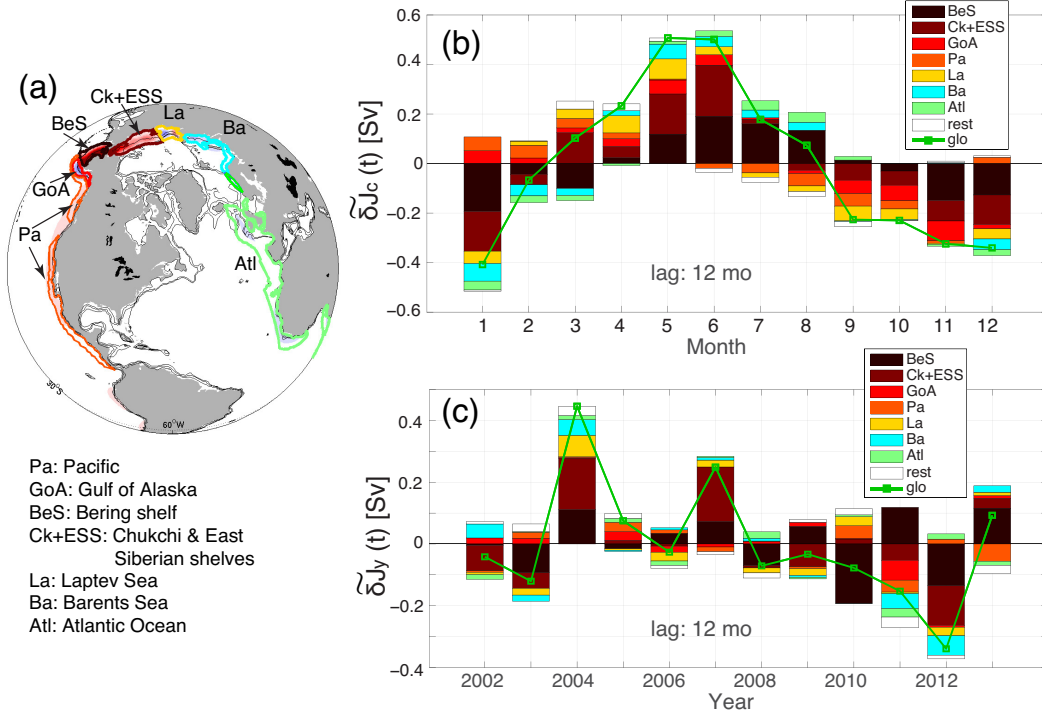
Figure 6. (a) Partition of regions of influence based on ocean regions and along important continental shelves. Reconstructions, using only $\delta\tau_{[N,E]}$ of (b) $\widetilde{\delta J_c}$ and (c) $\widetilde{\delta J_y}$ as a function of regional contributions. In (b-c), "rest" refers to the rest of the ocean excluding those regions highlighted in (a), and "glo" is the global sum. Panel (a) also links region abbreviations to their geographical location.

During the two extreme years, 2004 and 2012, contributions from the combined La and Ba are more prominent. Annual transport anomalies for these two years, in addition to 2007, are the primary factors determining the decline in the model annual transports between 2002–2013, and may have some bearing on the difference between the model and observed trends.

The relationship between the extreme years and the regional contribution give insight into the debate as to whether Bering Strait throughflow variability is forced from the Pacific in the direction of the mean flow through the strait (which is northward) or the Arctic/Atlantic. The traditional view of the dominance of Pacific origin forcing has been recently challenged (Peralta-Ferriz & Woodgate, 2017). Fig. 7 splits the contributions shown in Fig. 6 into Pacific and Arctic/Atlantic components. Seasonally (Fig. 7b), the results support the conclusion of Peralta-Ferriz and Woodgate (2017), that the summer transport variability is more strongly related to perturbations over the Arctic, although the Pacific-forced component remains significant. During fall, forcing over the Pacific is more important, although forcing over the Arctic still plays a significant role. Interannually (Fig. 7c), both Pacific and Arctic/Atlantic forcings provide significant contributions. Where their influences are coherent, extrema in transports are typically found (2004, 2007, 2012). However, the Arctic/Atlantic contributions are generally larger and more highly correlated with the total annual anomaly (correlation coefficient $\rho(\widetilde{\delta J}_{Arctic/Atlantic}, \delta J_{fwd}) = 0.94$, compared to $\rho(\widetilde{\delta J}_{Pacific}, \delta J_{fwd}) = 0.74$), and can usually predict the sign of the total anomaly (with the exception being the year 2010).
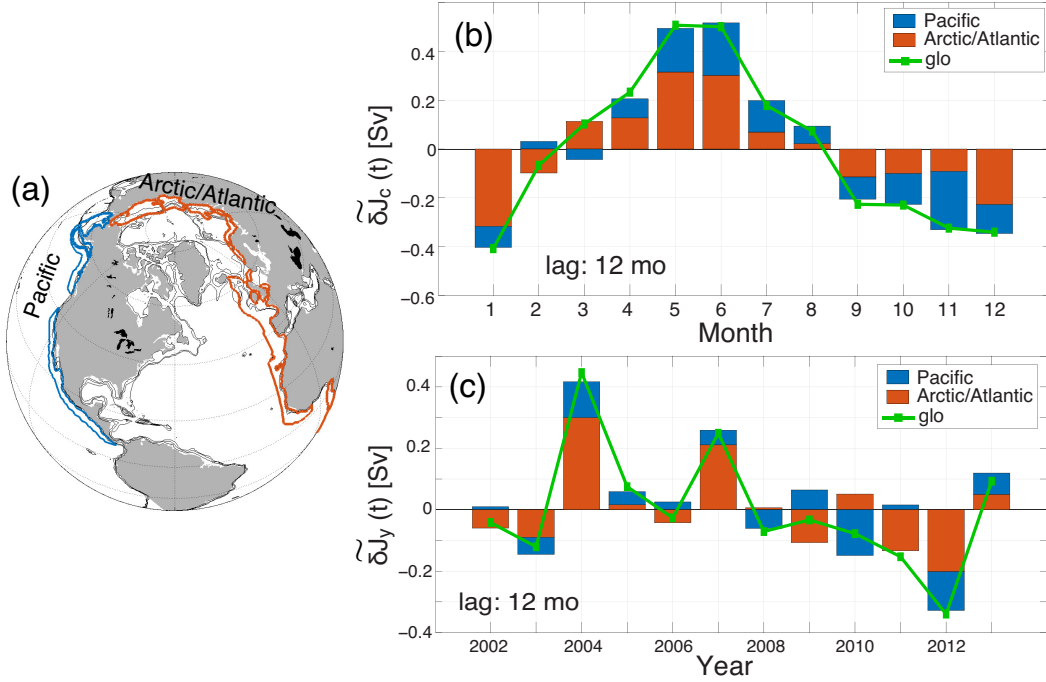
Figure 7. Same as Fig. 6, but partitioned in terms of contributions from the Pacific (south of the strait, blue) and Arctic/Atlantic sectors (north of the strait, orange).
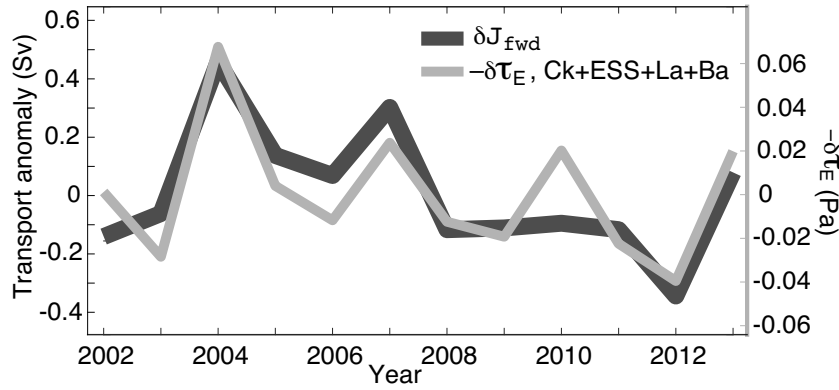

Figure 8. Minus eastward wind stress anomalies (light-gray, right y-axis) and transport anomalies (left y-axis) for the forward run (δJ_{fwd}, thick dark gray).

We can go one step further and inspect the individual forcing anomalies in the eight regions highlighted in Fig 6 to identify if any particular distribution of regional forcing anomalies determine the three years of the transport extrema (2004, 2007, and 2012). One strong correlation (correlation coefficient of 0.84) can be identified, as shown in Fig. 8, between the combined $\delta\tau_E$ for the combined regions Ck+ESS+La+Ba (grey) and the annual Bering Strait transport anomalies δJ (black line). Given the corresponding peaks (positive and negative) of $\delta\tau_E$ and δJ, we can deduce that large τ_E anomalies in the regions north of the Bering Strait (Ck+ESS+La+Ba) are responsible for the extrema in the model δJ. To confirm this, we performed a series of perturbation experiments, in which we replaced wind stress in years of extrema with that from the the prior years, and restrict the perturbed forcing to only within these regions. Our results (not shown) con-
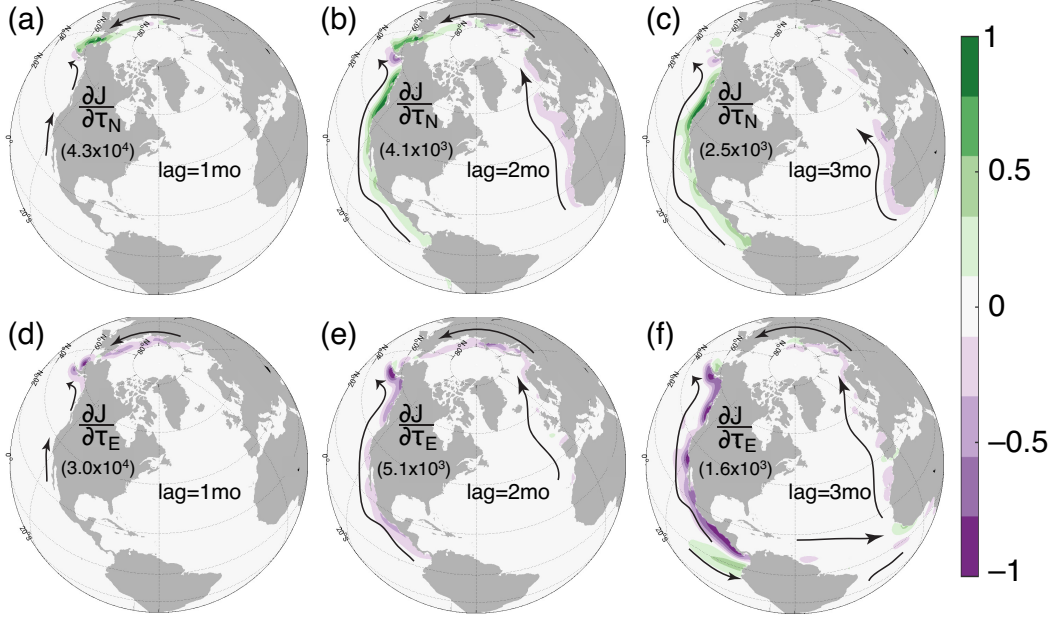
Figure 9. Normalized sensitivity (factor given on each plot) to τ_N (a-c) and τ_E (d-f) for lags of 1–3 months (columns). Arrows indicate direction of propagation of Kelvin and shelf waves. Geographical influence in time (reaching from the Pacific/Atlantic oceans in 2 months, and from the equator at 3 months lags) are consistent with wave phase speed estimates as discussed in the text. Note that scale factor varies by a factor of $\sim$20 across the different lags.

firm that wind stress anomalies in several key identified regions are primary controlling factors in determining the transport results in the model. The result also underlines the importance of improving the accuracy of wind stress in atmospheric reanalyses.

4 Discussion

4.1 Regions of Influence

Our work suggests the dominant forcing of Bering Strait transport anomalies to be localized and with only limited time lag. Nevertheless, there are also remote, longer timescale influences, as shown by Fig. 6. Continental shelf waves and coastally trapped Kelvin waves have been suggested as important mechanisms for transferring perturbations along coasts in general, (e.g. Brink, 1991; Heimbach et al., 2011; Pillar et al., 2016). Using observations, atmospheric reanalyses, statistical analyses and idealized models, Danielson et al. (2014) found evidence suggesting Kelvin and coastal shelf waves as playing an important role in influencing the Bering Strait throughflow variations. In our result, the sensitivity patterns are consistent with propagation directions of such waves in the northern hemisphere (i.e., with the coast to their right), with the important regions of influence all located upstream in the Kevin/shelf wave-propagation sense of the strait. As discussed in Section 2.1, both wavelengths and phase speeds of these waves may be modified due to numerical effects associated with grid-spacing aliasing and instability damping. The adjoint sensitivities shown here inherit such numerical modifications, and are thus reflecting these modified coastal waves. Fig. 9 shows the sensitivities of δJ to wind stress, now highlighting the directions of Kelvin/shelf wave propagation that can contribute to positive δJ. For each subplot, the sensitivity is normalized by its maximum magnitude at each corresponding lag to highlight the spatial distribution and time-scale

of propagation along the coastal regions. We ask next if the timescales are reasonable, while keeping in mind the modified numerical representation of these waves.

Previous observational-based studies of multi-decadal sea surface height records along the Siberian and Laptev Sea Shelves showed presence of shelf waves with phase velocities of 1.3 to 5.2 m/s and periods of less than 60 days associated with synoptic wind perturbations (Voinov & Zakharchuk, 1999). Further away in the Barents Sea and along the Norwegian coast, numerical and theoretical calculations by Drivdal et al. (2016) support evidence of the presence of coastal Kelvin waves and continental shelf waves generated by atmospheric storms with a phase speed of 5–24 m/s and a period ∼44 hours. Estimating the length of the east Siberian and Laptev Sea Shelves as ∼4600 km yields a timescale of about 10–40 days for coastal shelf waves originated from these shelves to reach Bering Strait. In the model, sensitivities associated with the expected damped phase speeds are seen with lags within 1 month (Fig. 9a), which can be interpreted as consistent with the observed timing of ∼10+ days for fast shelf waves plus numerically induced delay. Similarly, the additional distance to traverse along the coast in the Barents and Nordic Seas of 8000 km at wave phase speeds 5–24 m/s yields an additional 4–20 days. Thus, for fast waves, the theoretical travel time from south of the Nordic Seas to Bering Strait is ∼14 days. Model sensitivities indicate that it takes less than two months for waves which originated along these coastal regions to reach the Bering Strait (Fig. 9b). Again, considering the expected damped phase velocities suggests shelf waves in the faster range associated with transit time ∼14+ days plus delay as the likely mechanism.

Within three months, sensitivities can be traced to the equatorial Kelvin wave-guide paths (wave phase speed ∼1–3 m/s estimated by Eriksen et al., 1983 over a distance ∼7300 km, yielding a transit time of 28–84 days, or twice the duration if we assume a 50% underestimation of the phase velocity in the model) in both the Pacific and Atlantic Oceans (Heimbach et al., 2011). As information is more dispersed spatially, the magnitude of sensitivities decreases such that the total contributions of all regions to wind perturbations at this lag only contribute ∼1% to the total Bering Strait transport. Note that the high or low sensitivity by itself does not solely determine the magnitude of the contribution to transport δJ from that region, since the final contribution to transport depends on the sum through various lags of the product of sensitivity and the forcing anomaly.

In terms of wind stress magnitude and direction, as indicated by the color scale in Fig. 9, northwestward wind stress (positive τ_N, negative τ_E) along the coast in the Pacific contribute primarily to positive increase in $\widetilde{\delta J}$ at Bering Strait. Similarly, along the coast of the East Siberian and Laptev Seas, northwestward wind stress gives positive $\widetilde{\delta J}$. At further distance from the strait in the Arctic/Atlantic sector, along the coast in the Barents and Nordic Seas and in the eastern margin of the Atlantic Ocean, southwestward wind stress contribute to positive $\widetilde{\delta J}$. This is consistent with results from Peralta-Ferriz and Woodgate (2017) which show that winds that invoke onshore (offshore) Ekman flow in the Bering+Pacific sector (Arctic + Barents + Nordic + Atlantic sector) are related to positive flow anomalies at the strait.

4.2 The Effect of Precipitation

The majority of work in this paper has focused on the impacts of wind stress anomalies on the flow variations through the strait, as that was found to be the greatest driver in the adjoint experiments performed. The method, however, allows us to examine the impact of other forcings as well – e.g., precipitation which is also hypothesized to be a driver of the Bering Strait throughflow variability (Stigebrandt, 1984).

Fig. 10 shows the sensitivity of the Bering Strait transport anomaly to precipitation perturbations for lags ranging from 1 month to 10 years. Summing these shows the total contribution to Bering Strait flow variability to be small (order of 0.01 Sv). Nevertheless, the patterns are themselves interesting. At 1 month lag, Bering Strait flow is
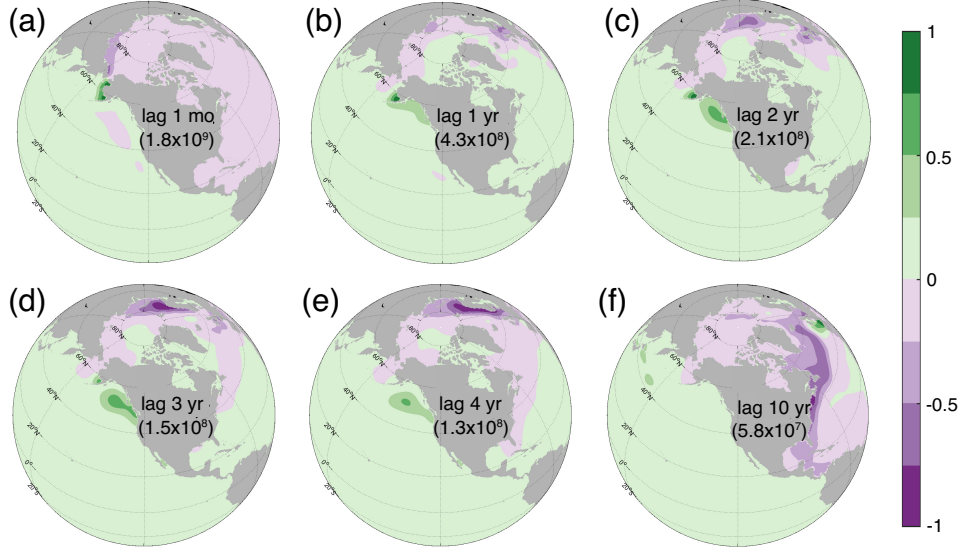
Figure 10.   (a) Normalized adjoint sensitivity to precipitation (positive precipitation implies adding freshwater to the ocean) for time lags from 1 month to 10 years. The normalization factor is the maximum magnitude of sensitivity at each lag and is given on each plot. Note that the normalization factor varies by a factor of ∼30 across the plots.

enhanced by positive net precipitation over the Bering Sea Shelf and negative net precipitation over the east Siberian Sea. This pattern enhances the steric sea surface slope through the strait, mechanistically increasing northward flow, as per the steric driving of the flow due to the global freshwater cycle as suggested by Stigebrandt (1984). At longer lags of 1–4 years, the region of sensitivity to positive precipitation is further south (along the Alaskan Coast) while the region where negative precipitation enhances the flow now extends further along the Russian coast and into the Bering Sea. Note that these lags are much larger than the few-month lags for wind stress forcings, indicative of the difference between the wave phase speeds of a few m/s and mean ocean circulation speeds of order of a few cm/s.

Precipitation influences emerge along the Gulf Stream paths in the North Atlantic after 3 years (Fig. 10d-f) and along the Kuroshio path in the North Pacific after 4 years (Fig. 10e-f). In general, the sign of the sensitivity is consistent with the steric "pressure head" hypothesis (Stigebrandt, 1984) that negative (positive) precipitation anomalies δP into the Atlantic (Pacific) Ocean would increase the steric sea surface height difference between the two oceans and promote increased in δJ at the strait. However, given that the magnitude of $\partial J/\partial P$ of $O(10^9)$ (m³/s)/(m/s) and that δP is of the order $O(10^{-8})$ m/s, δJ_P is of the order $O(10^1)$ m³/s or $(10^{-5}$ Sv) which is significantly smaller than contributions from wind stress, we conclude that these patterns, though interesting, are not of much relevance, and advective/wind-driven effects are a much larger forcing of the Bering Strait throughflow than the steric term, at least on timescales of months to years, as De Boer and Nof (2004a, 2004b) have suggested. Note that since we are considering anomalies, we cannot draw direct conclusions about the forcing of the **mean** of the Bering Strait transport, which may still have a significant steric contribution.

5 Conclusions

The ECCOv4r2 forward and adjoint models were used to investigate the mechanisms controlling the variability of the Bering Strait throughflow. Adjoint sensitivities show that the model's Bering Strait transport anomaly is controlled primarily by the wind stress on short time-scales of order 0–5 months, with the percentage of explained monthly variance of the flow being ∼90% and 92% within the first month and the first five months, respectively. Other atmospheric forcing terms (precipitation, radiative fluxes, water vapor content, air temperature) have negligible (< 1%) influence on both short (monthly) and long (interannual) variability.

Spatial decomposition indicates that on short time scales (monthly) winds over the Bering Shelf and the combined Chukchi and East Siberian regions are the most significant drivers. Each region contributes approximately equal amounts in magnitudes to the net transport anomalies (∼ 40% each), with the combined Chukchi and East Siberian regions being slightly more influential. Sensitivity patterns indicative of coastally trapped adjoint wave propagation lead us to hypothesize that continental shelf waves and coastally-trapped waves are the dominant mechanisms for propagating information from upstream (in the Kelvin wave-propagation sense) to the strait. Further support for this hypothesis comes from a reasonable match of timescales of propagation of influences with wave phase speed estimates from the literature and findings from prior work by Danielson et al. (2014) and others, after potential numerical damping of the model's fast waves is taken into account.

Including wind-stress influence from regions further away from the strait in the reconstruction yields a similar conclusion that the Bering Sea Shelf, the Chukchi Sea, and the East Siberian Sea remain the dominant drivers of the Bering Strait flow variability (80% combined), with additional contribution of influences from the Barents and Nordic Seas, the eastern Pacific Ocean and eastern Atlantic Ocean (Fig. 6). These far field influences contribute ∼20% of the monthly-scale variability (Fig. 5b) and ∼30% of the seasonal variability (Fig. 6b).

To address the long standing question as to whether the flow variability is driven from the Pacific or the Arctic/Atlantic sector, influences of forcing anomalies from these two regions were compared. Results show that both sectors are important, and that extrema in transports occur when their influences act in concert. Interestingly, the Arctic/Atlantic forcings are better predictors of anomalous flow than those over the Pacific (correlation coefficient $\rho(\widetilde{\delta J}_{Arctic/Atlantic}, \delta J_{fw}) = 0.94$ compare to $\rho(\widetilde{\delta J}_{Pacific}, \delta J_{fw}) = 0.74$). An important conclusion is the recognition that the Arctic shelves act as efficient conduits and play a substantial role in determining the Bering Strait flow variability. Our results support previous findings (De Boer & Nof, 2004a, 2004b) of the importance of basin-scale winds (Peralta-Ferriz & Woodgate, 2017) in driving the Bering Strait transport variability. They also show that the contribution of net freshwater fluxes (precipitation and runoff minus evaporation) contributes very little (< 1%) to the transport variability.

In contrast to previous work, which is based on simple theoretical or statistical models, our results are based on the use of the dynamically and kinematically consistent state-estimation framework and the detailed analysis of adjoint model-derived sensitivities to conduct dynamical attributions. These results yield more physical insight than is conventionally obtained from purely statistical methods. Our findings of the impact of local and far field forcings on the flow substantially advance our understanding of the mechanisms driving transport variability at the Bering Strait. Another key finding is the importance of the Arctic (especially the Chukchi and the East Siberian and Laptev Seas) on the flow variability, contrasting the prior assumptions that the flow is driven primarily from south of the strait. Lastly, the short-term and localized response of the strait

⁷³⁶ transport anomalies to the forcing suggests some predictive skill if sufficiently accurate
⁷³⁷ wind stress fields, especially in the Arctic, are available.

Acknowledgments

This work was supported by NSF OPP grants 1304050 and 1603903, and by NSF Arctic Observing Network grants PLR-1304052 and PLR 1758565. Additional support for PH came from a JPL/Caltech subcontract for the "Estimating the Circulation and Climate of the Ocean" project. The Bering Strait mooring data are freely available via the Bering Strait Observing Network website (psc.apl.washington.edu/BeringStrait.html) and the permanent US oceanographic data archives at the National Centers for Environmental Information (www.nodc.noaa.gov). The ECCOv4r2 model setup used in this work can be accessed from public repositories and permanent archives (Campin et al., 2019; Forget, 2016a, 2016b, 2018). Adjoint code was generated using the TAF software tool, created and maintained by FastOpt GmbH (http://www.fastopt.com/). We thank two anonymous reviewers for comments that greatly improved the manuscript.

References

Adcroft, A., Campin, J., Dutkiewicz, S., Evangelinos, C., Ferreira, D., Forget, G., . . . Molod, A. (2018). *MITgcm user manual.* doi: 1721.1/117188

Adcroft, A., & Campin, J.-M. (2004). Rescaled height coordinates for accurate representation of free-surface flows in ocean circulation models. *Ocean Modelling*, *7*(2004), 269–284. doi: 10.1016/j.ocemod.2003.09.003

Adcroft, A., Hill, C., & Marshall, J. (1997). Representation of topography by shaved cells in a height coordiate ocean model. *Mon. Wea. Rev.*, *125*, 2293–2315.

Arrigo, K. R. (2014). Sea ice ecosystems. *Annual Review of Marine Science*, *6*(1), 439-467. (PMID: 24015900) doi: 10.1146/annurev-marine-010213-135103

Arrigo, K. R., Perovich, D. K., Pickart, R. S., Brown, Z. W., van Dijken, G. L., Lowry, K. E., . . . Swift, J. H. (2012). Massive phytoplankton blooms under Arctic sea ice. *Science*. doi: 10.1126/science.1215065

Brink, K. (1991). Coastal-trapped waves and wind-driven currents over the continental shelf. *Annu. Rev. Fluid Mech.*, *23*, 389–412.

Campin, J.-M., Adcroft, A., Hill, C., & Marshall, J. (2004). Conservation of properties in a free-surface model. *Ocean Modelling*, *6*, 221–244. doi: 10.1016/S1463 -5003(03)00009-X

Campin, J.-M., Heimbach, P., Losch, M., Forget, G., Hill, E., Adcroft, A., . . . McRae, A. T. T. (2019). *MITgcm/MITgcm: checkpoint67m.* Zenodo. doi: 10.5281/zenodo.3492298

Casulli, V., & Cattani, E. (1994). Stability, accuracy, and efficiency of a semi-implicit method for three-dimensional shallow water flow. *Computers Math. Applic.*, *27*(4), 99–112.

Cavalieri, D. J., Crawford, J., Drinkwater, M. R., Eppler, D., Farmer, L. D., Jentz, R. R., & Wackerman, C. C. (1991). Aircraft active and passive microwave validation of sea ice concentration from the DMSP SSM/I. *Journal of Geophysical Research*, *96*(C12), 21989–22009.

Chaudhuri, A., Ponte, R., Forget, G., & Heimbach, P. (2013). A comparison of atmospheric reanalysis surface products over the ocean and implications for uncertainties in air-sea boundary forcing. *J. Climate*, *26*, 153–170. doi: JCLI-D-12-00090.1

Chaudhuri, A., Ponte, R., & Nguyen, A. (2014). A comparison of atmospheric reanalysis products for the Arctic Ocean and implications for uncertainties in air-sea fluxes. *J. Climate*, *27*(14), 5411–5421. doi: http://dx.doi.org/10.1175/ JCLI-D-13-00424.1

Coachman, L., & Aagaard, K. (1966). On the water exchange through Bering Strait. *Limonology and Oceanogr.*, *11*(1), 44–59. doi: 10:4319/lo.1966.11.1.0044

Danielson, S. L., Weingartner, T. J., Hedstrom, K. S., Aagaard, K., Woodgate, R. A., Chuchitser, E., & Stabeno, P. J. (2014). Coupled wind-forced controls of the Bering-Chukchi shelf circulation and the Bering Strait through-

flow: Ekman transport, continental shelf waves, and variations of the Pacific-Arctic sea surface height gradient. *Progress in Oceanogr.*, *125*, 40–61. doi: http://dx.doi.org/10.1016/j.pocean.2014.04.006

De Boer, A., & Nof, D. (2004a). The Bering Strait's grip on the northern hemisphere climate. *Deep-Sea Res., Part I*, *51*(10), 1347–1366. doi: 10.1016/j.dsr.2004.05.003

De Boer, A., & Nof, D. (2004b). The exhaust valve of the North Atlantic. *J. Climate*, *17*(3), 417–422. doi: 10.1175/1520-0442

Dee, D. P., Uppala, S. M., Simmons, A. J., Berrisford, P., Poli, P., Kobayashi, S., . . . Vitart, F. (2011). The ERA-Interim reanalysis: configuration and performance of the data assimilation system. *Q. J. R. Meteorol. Soc.*, *137*(656), 553–597. doi: 10.1002/qj.828

Drivdal, M., Weber, J., & Debernard, J. (2016). Dispersion relation for continental shelf waves when the shallow shelf part has an arbitrary width: Application to the shelf west of Norway. *Journal of Physical Oceanography*, *46*(2), 537-549. doi: 10.1175/JPO-D-15-0023.1

Eriksen, C., Blumenthal, M., Hayes, S., & Ripa, P. (1983). Wind-generated equatorial Kelvin waves observed across the Pacific Ocean. *Journal of Physical Oceanography*, *13*, 1622–1640.

Fenty, I., & Heimbach, P. (2013). Coupled sea ice-ocean state estimation in the Labrador Sea and Baffin Bay. *J. Phys. Ocean.*, *43*(6), 884–904. doi: 10.1175/JPO-D-12-065.1

Fenty, I., Menemenlis, D., & Zhang, H. (2015). Global coupled sea ice-ocean state estimate. *Clim. Dyn..* doi: 10.1007/s00382-015-2796-6

Forget, G. (2016a). *ECCO version 4 release 2 inputs: model initialization.* Harvard Dataverse. doi: 10.7910/DVN/7XYXSF

Forget, G. (2016b). *ECCO version 4 release 2 inputs: surface forcing fields.* Harvard Dataverse. doi: 10.7910/DVN/9WYSZF

Forget, G. (2018). *gaelforget/eccov4: Documentation updates.* Zenodo. doi: 10.5281/zenodo.1211363

Forget, G., Campin, J. M., Heimbach, P., Hill, C. N., Ponte, R. M., & Wunsch, C. (2015). ECCO version 4: an integrated framework for non-linear inverse modeling and global ocean state estimation. *Geosci. Model Dev.*, *8*, 3071-3104. doi: 10.5194/gmd-8-3071-2015

Fukumori, I., Heimbach, P., Ponte, R. M., & Wunsch, C. (2018). A dynamically consistent, multi-variable ocean climatology. *Bulletin of the American Meteorological Society.* doi: 10.1175/BAMS-D-17-0213.1

Fukumori, I., Wang, O., Llovel, W., Fenty, I., & Forget, G. (2015). A near-uniform fluctuation of ocean bottom pressure and sea level across the deep ocean basins of the Arctic Ocean and the Nordic Seas. *Progress in Oceanography*, *134*(C), 152–172.

Griffiths, S. D. (2013). Kelvin wave propagation along straight boundaries in C-grid finite-difference models. *Journal of Computational Physics*, *255*, 639–659. doi: http://dx.doi.org/10.1016/j.jcp.2013.08.040

Heimbach, P., Fukumori, I., Hill, C. N., Ponte, R. M., Stammer, D., Wunsch, C., . . . Zhang, H. (2019). Putting it all together: Adding value to the global ocean and climate observing systems with complete self-consistent ocean state and parameter estimates. *Frontiers in Marine Science*, *6*, 769–10.

Heimbach, P., Menemenlis, D., Losch, M., Campin, J., & Hill, C. (2010). On the formulation of sea-ice models. Part 2: Lessons from multi-year adjoint sea-ice export sensitivities through the Canadian Arctic Archipelago. *Ocean Modeling*, *33(1-2)*, 145-158. doi: 10.1016/j.ocemod.2010.02.002

Heimbach, P., Wunsch, C., Ponte, R. M., Forget, G., Hill, C., & Utke, J. (2011). Timescales and regions of the sensitivity of Atlantic meridional volume and heat transport: Toward observing system design. *Deep Sea Research*

Part II: Topical Studies in Oceanography, *58*(17-18), 1858–1879.   doi: 10.1016/j.dsr2.2010.10.065

Hsieh, W. W., Davey, M. K., & Wajsowicz, R. C.   (1983).   The free Kelvin wave in finite-difference numerical models. *J. Phys. Oceanogr.*, *13*, 1383–1397.

Hu, A., & Meehl, G. (2005). Bering Strait throughflow and the thermohaline circulation. *Geophys. Res. Lett.*, *32*(L24610). doi: 10.1029/2005GL024424

Hu, A., Meehl, G., Han, W., Timmermann, A., Otto-Bliesner, B., Liu, Z., . . . Wu, B.   (2012).   Role of the Bering Strait on the hysteresis of the ocean conveyor belt circulation and glacial climate stability.   *Proceedings of the National Academy of Sciences of the United States of America*, *109*(17), 6417–6422. doi: 10.1073/pnas.1116014109

Kalnay, E., Kanamitsu, M., Kistler, R., Collins, W., Deaven, D., Gandin, L., . . . Reynolds, R.   (1996).   The NCEP/NCAR 40-Year reanalysis project. *Bulletin of the American Meteorological Society*, *77*(3), 437-471.   doi: 10.1175/1520-0477(1996)077⟨0437:TNYRP⟩2.0.CO;2

Kawai, Y., Osafune, S., Masuda, S., & Komuro, Y.   (2018).   Relations between salinity in the northwestern Bering Sea, the Bering Strait throughflow and sea surface height in the Arctic Ocean. *Journal of Oceanography*, *74*, 239–261. doi: https://doi.org/10.1007/s10872-017-0453-x

Kinney, J. C., Maslowski, W., Aksenov, Y., de Cuevas, B., Nguyen, A., Osinski, R., . . . Zhang, J.   (2014).   On the flow through Bering Strait: a synthesis of model results and observations.   In J. Grebmeier & W. Maslowski (Eds.), (pp. 167–198). Dordrecht: Springer Dordrecht.

Kobayashi, S., Ota, Y., Harada, Y., Ebita, A., Moriya, M., Onoda, H., . . . Takahashi, K.   (2015).   The JRA-55 reanalysis: General specifications and basic characteristics. *Journal of the Meteorological Society of Japan*, *93*(1), 5–48.

Kurihara, Y. (1965). On the use of implicit and iterative methods for the time integration of the wave equation. *Monthly Weather Review*, *93*(1), 33–46.

Lammers, R. B., & Shiklomanov, A. I.   (2001).   Assessment of contemporary Arctic river runoff based on observational discharge records.   *J. Geophys. Res.*, *106*(D4), 3321.

Marshall, J., Adcroft, A., Hill, C., Perelman, L., & Heisey, C.   (1997).   A finite-volume, incompressible Navier Stokes model for studies of the ocean on parallel computers. *J. Geophys. Res.*, *102*, 5753–5766.

Nguyen, A. T., Menemenlis, D., & Kwok, R.   (2011).   Arctic ice-ocean simulation with optimized model parameters: approach and assessment. *J. Geophys. Res.*, *116*. doi: 10.1029/2010JC006573

Onogi, K., Tsutsui, J., Koide, H., Sakamoto, M., Kobayashi, S., Hatsushika, H., . . . Taira, R.   (2007).   The JRA-25 reanalysis.   *J. Meteor. Soc. Japan*, *85*(3), 369–432.

Peralta-Ferriz, A. C., & Woodgate, R. A.   (2017).   The dominant role of the East Siberian Sea in driving the oceanic flow through the Bering Strait - Conclusions from GRACE ocean mass satellite data and in situ mooring observations between 2002 and 2016. *Geophysical Research Letters*, *44*, 11,472–11,481. doi: 10.1002/2017GL075179

Pillar, H., Heimbach, P., Johnson, H., & Marshall, D. (2016). Dynamical attribution of recent variability in Atlantic overturning.   *J. Clim.*, *29*, 3339–3352.   doi: 10.1175/JCLI-D-15-0727.1

Roemmich, D., Johnson, G., Riser, S., Davis, R., Gilson, J., Owens, W., . . . Ignaszewski, M.   (2009).   The Argo program: Observing the global ocean with profiling floats. *Oceangraphy*, *22*(2), 34-44. doi: 10.5670/oceanog.2009.36

Schwab, D. J., & Beletsky, D.   (1998).   Propagation of Kelvin waves along irregular coastlines in finite-difference models.   *Advances in Water Resources*, *22*(3), 239–245.

Serreze, M. C., Barrett, A. P., Slater, A. G., Steele, M., Zhang, J., & Trenberth,

K. E. (2007). The large-scale energy budget of the Arctic. *J. Geophys. Res.*, *112*(C11122). doi: 10.1029/2006JD008230

Serreze, M. C., Barrett, A. P., Slater, A. G., Woodgate, R. A., Aagaard, K., Lammers, R. B., . . . Lee, C. M. (2006). The large-scale freshwater cycle of the Arctic. *J. Geophys. Res.*, *111*(C11010). doi: 10.1029/2005JC003424

Serreze, M. C., Crawford, A. D., Stroeve, J., Barrett, A. P., & Woodgate, R. A. (2016). Variability, trends, and predictability of seasonal sea ice retreat and advance in the Chukchi Sea. *J. of Geophys. Res..* doi: 10.1002/2016jc011977

Shiklomanov, A. I., Yakovleva, T. I., Lammers, R. B., Karasev, I. P., Vörösmarty, C. J., & Linder, E. (2006). Cold region river discharge uncertainty—estimates from large Russian rivers. *Journal of Hydrology*, *326*(1-4), 231–256.

Smith, T., & Heimbach, P. (2018). Atmospheric origins of variability in the South Atlantic meridional overturning circulation. *Journal of Climate*, *32*, 1483–1500. doi: https://doi.org/10.1175/JCLI-D-18-0311.1

Stammer, D. (2005). Adjusting internal model errors through ocean state estimation. *J. Phys. Oceanogr.*, *35*(6), 1143–1153.

Stammer, D., Balmaseda, M., Heimbach, P., Köhl, A., & Weaver, A. (2016). Ocean data assimilation in support of climate applications: Status and perspectives. *Annu. Rev. Mar. Sci.*, *8*(1), 491–518. doi: 10.1146/annurev-marine-122414 -034113

Steele, M., & Ermold, W. (2007). Steric sea level change in the Northern Seas. *Journal of Climate*, *20*, 403–417.

Stigebrandt, A. (1984). The North Pacific: a global-scale estuary. *J. Phys. Oceanogr.*, *14*(2), 464–470.

Toole, J., Krishfield, R., Proshutinsky, A., Ashjian, C., Doherty, K., Frye, D., . . . Shanahan, T. (2006). Ice-tethered profilers sample the upper Arctic Ocean. *EOS Trans. AGU*, *87*(41), 434–3.

Toulany, B., & Garrett, C. (1984). Geostrophic control of fluctuating barotropic flow through straits. *Journal of Physical Oceanography*, *14*(4), 649-655. doi: 10 .1175/1520-0485(1984)014⟨0649:GCOFBF⟩2.0.CO;2

Uppala, S. M., KAllberg, P. W., Simmons, A. J., Andrae, U., Bechtold, V. D. C., Fiorino, M., . . . Woollen, J. (2005). The ERA-40 re-analysis. *Quarterly Journal of the Royal Meteorological Society*, *131*(612), 2961–3012. doi: 10.1256/qj.04.176

Voinov, G., & Zakharchuk, E. (1999). Large-Scale variations of sea level in the Laptev Sea. In H. Kassens et al. (Eds.), (pp. 25–36). Berlin, Heidelberg: Springer Berlin Heidelberg.

Wadley, M. R., & Bigg, G. R. (2002). Impact of flow through the Canadian Archipelago and Bering Strait on the North Atlantic and Arctic circulation: An ocean modelling study. *Quarterly Journal of the Royal Meteorological Society*, *128*(585), 2187–2203. Retrieved from `http://dx.doi.org/10.1256/ qj.00.35` doi: 10.1256/qj.00.35

Walsh, J., Dieterle, D., Muller-Karger, F., Aagaard, K., Roach, A., Whitledge, T., & Stockwell, D. (1997). CO2 cycling in the coastal ocean. II. Seasonal organic loading of the Arctic Ocean from source waters in the Bering Sea. *Continental Shelf Research*, *17*(1), 1–36.

Weingartner, T., Danielson, S., & Royer, T. (2005). Freshwater variability and predictability in the Alaska Coastal Current. *Deep Sea Research II*, *52*, 169–191.

Woodgate, R. A. (2018). Increases in the Pacific inflow to the Arctic from 1990 to 2015, and insights into seasonal trends and driving mechanisms from year-round Bering Strait mooring data. *Progress in Oceanography*, *160*, 124–154. doi: https://doi.org/10.1016/j.pocean.2017.12.007

Woodgate, R. A., Aagaard, K., & Weingartner, T. J. (2005a). Monthly temperature, salinity, and transport variability of the Bering Strait through flow. *Geophys. Res. Lett.*, *32*(L04601). doi: 10.1029/2004GL021880

Woodgate, R. A., Aagaard, K., & Weingartner, T. J.   (2005b).   A year in the physical oceanography of the Chukchi Sea: Moored measurements from autumn 1990-1991.   *Deep-Sea Res., Part II*, *52*(24–26), 3116–3149.   doi: 10.1016/j.dsr2.2005.10.016

Woodgate, R. A., Aagaard, K., & Weingartner, T. J. (2006). Interannual changes in the Bering Strait fluxes of volume, heat and freshwater between 1991 and 2004. *Geophys. Res. Lett.*, *33*(L15609), 10.1029/2006GL026931.

Woodgate, R. A., Stafford, K. J., & Prahl, F. G.   (2015).   A synthesis of year-round interdisciplinary mooring measurements in the Bering Strait (1990–2014) and the RUSALCA years (2004–2011).   *Oceanography*, *28*(3), 46–67.   doi: 10.5670/oceanog.2015.57

Woodgate, R. A., Weingartner, T., & Lindsay, R.   (2010).   The 2007 Bering Strait oceanic heat flux and anomalous Arctic sea-ice retreat.   *Geophys. Res. Lett.*, *37*(L01602). doi: 10.1029/2009GL041621

Woodgate, R. A., Weingartner, T., & Lindsay, R.   (2012).   Observed increases in Bering Strait oceanic fluxes from the Pacific to the Arctic from 2001 to 2011 and their impacts on the Arctic Ocean water column.   *Geophys. Res. Lett.*, *39*(L24603). doi: 10.1029/2012GL054092

Wunsch, C., & Heimbach, P. (2007). Practical global oceanic state estimation. *Physica D: Nonlinear Phenomena*, *230*(1-2), 197–208. doi: 10.1016/j.physd.2006.09.040

Wunsch, C., & Heimbach, P.   (2013).   Dynamically and kinematically consistent global ocean circulation and ice state estimates.   In *Ocean circulation and climate: A 21st century perspective* (pp. 553–579).   Elsevier Ltd.   doi: 10.1016/B978-0-12-391851-2.00021-0

Supporting Information for "Elucidating large-scale atmospheric controls on Bering Strait throughflow variability using a data-constrained ocean model and its adjoint"

An T. Nguyen[1], Rebecca A. Woodgate[2], and Patrick Heimbach[1]

[1]University of Texas at Austin, Austin, TX, USA

[2]University of Washington, Seattle, WA, USA

Contents of this file

Introduction

The materials included here (i) clarify the choice of the timing of when the quantity of interest, i.e. the Bering Strait transport, is defined, and (ii) provide of full derivation of the formulation used to decompose the Bering Strait transport anomaly time-series into temporal components.

—————

1. Dependence of reconstruction of $\widetilde{\delta J}$ on the time when J is defined

The monthly mean transport $J(t_i)$ for each month t_i has large variability with negative values (southward flow) during some months and maximum positive values during other months (Fig. S1a). An important question is whether and how the gradients $\frac{\partial J}{\partial \Omega_k}$ vary when J varies. Intuitively we expect that if there is a dominant linear mechanism controlling the transport, the gradient $\frac{\partial J}{\partial \Omega_k}$ retains the same sign and similar magnitude, independent of the period over which J is defined. For example, if northward wind stress is the dominant controlling mechanism such that $\frac{\partial J}{\partial \tau_N} = X$, a smaller J is then a result of weaker τ_N and a negative J is a result of a reversal of the wind stress (negative τ_N). Thus, J can vary widely and is a result of the variation in τ_N, while the physical connection, as captured by $\frac{\partial J}{\partial \tau_N} = X$, remains the same.

Following this line of argument, we hypothesize that if instead $\frac{\partial J}{\partial \Omega_k}$ is dependent on the time when J is defined (e.g., phase of the seasonal cycle), it is due to J being a highly non-linear function of Ω_k along the model trajectory such that at any given time the linearized gradients $\frac{\partial J}{\partial \Omega_k}$ cannot fully capture the physics. We can test this dependency by comparing gradients computed from different J for each forcing variable. Most importantly, we can compare the reconstructed $\widetilde{\delta J}$ using the corresponding gradients to see the impact of varying J on the reconstructed time series.

Gradients $\frac{\partial J}{\partial \Omega_k}$ were obtained from $J^{[07,09,12]}$ for three different averaged months that span the seasonal cycle [Jul/2013, Sep/2013, Dec/2013], and each was used to reconstruct the respective time-series $\widetilde{\delta J}^{[07,09,12]}$. These constructions as well as the forward anomaly time-series δJ_{fwd} are shown in Fig. S1. Linear fit of scatter plot of these various $\widetilde{\delta J}$ show

that they are different by up to **only 3%**, depending on the number of lags used in the reconstruction (Fig. S1b,c).

Thus, given that any of the reconstructed $\widetilde{\delta J}^{[07,09,12]}$ can capture the variability in the forward model δJ_{fwd} (Fig. S1a), that the difference between the these reconstructions is small, and that subsequent analyses show no significant differences in the behavior of how the reconstructions differ from the forward model time-series (Fig. S2), as discussed in the main text, we chose J^{09} for all gradients calculations and analyses in this study.

2. Reconstruction: temporal component derivations

Eqn. (3) can be used to reconstruct the full anomaly time series, $\widetilde{\delta J}$, which can then be decomposed into temporal components associated with interannual, seasonal, and monthly time-scales, as discussed in Section 3. Here we show that by rewriting eqn. (3), the reconstruction can be **approximated** as eqn. (4), which allows for more direct connection between the time-scales of the forcing anomalies and the time-scales of the Bering Strait transport anomalies. Our example here is for the reconstruction of the annual mean time series, but the same logic applies to other time-scales.

We first define the annual mean forcing $\delta\Omega_y$ for a year t_a within the time range $[t_a, t_a+T_y]$ as,

$$\delta\Omega_y(t_a) = \frac{1}{T_y} \int_{t_a}^{t_a+T_y} \delta\Omega(t)\, dt \tag{S.1}$$

where T_y is a time period of 1 year. Based on eqn. (3), the full reconstruction for the annual $\widetilde{\delta J}_y$ for the same year t_a at a specific geographic location $[x_1, x_2]$ for a forcing component k would be as follows, where for clarity we will omit the geographic integrals and location $[x_1, x_2]$ as well as the forcing index k from the equations, but the reader should

understand these integrals are still required. Note also that the sensitivity corresponding

to the first month $\frac{\partial J}{\partial \Omega(0)}$, i.e., where ($\alpha - t = 0$ mo), also termed the "zero-lag", is the

average of sensitivities accumulated between 0–1 month).

$$\widetilde{\delta J}_y(t_a) \tag{S.2}$$

$$= \frac{1}{T_y} \int_{t_a}^{t_a+T_y} \left[\int_{t_0}^{t} \frac{\partial J}{\partial \Omega}(\alpha - t)\delta\Omega(\alpha)d\alpha \right] dt$$

$$= \frac{1}{T_y} \int_{t_a}^{t_a+T_y} \left[\frac{\partial J}{\partial \Omega}(0)\delta\Omega(t) \qquad + \qquad \int_{t_0}^{t-1mo} \frac{\partial J}{\partial \Omega}(\alpha - t)\delta\Omega(\alpha)d\alpha \right] dt$$

$$= \frac{1}{T_y} \int_{t_a}^{t_a+T_y} \left[\frac{\partial J}{\partial \Omega}(0)\delta\Omega(t) \right] dt \quad + \frac{1}{T_y} \int_{t_a}^{t_a+T_y} \left[\int_{t_0}^{t-1mo} \frac{\partial J}{\partial \Omega}(\alpha - t)\delta\Omega(\alpha)d\alpha \right] dt$$

$$= \frac{\partial J}{\partial \Omega}(0)\frac{1}{T_y} \int_{t_a}^{t_a+T_y} \delta\Omega(t)dt \quad + \frac{1}{T_y} \int_{t_a}^{t_a+T_y} \left[\int_{t_0}^{t-1mo} \frac{\partial J}{\partial \Omega}(\alpha - t)\delta\Omega(\alpha)d\alpha \right] dt$$

$$= \frac{\partial J}{\partial \Omega}(0)\delta\Omega_y(t_a) \quad + \frac{1}{T_y} \int_{t_a}^{t_a+T_y} \left[\int_{t_0}^{t-1mo} \frac{\partial J}{\partial \Omega}(\alpha - t)\delta\Omega(\alpha)d\alpha \right] dt$$

$$= \frac{\partial J}{\partial \Omega}(0)\delta\Omega_y(t_a) \quad + \qquad\qquad\qquad \text{other terms}$$

The key rearrangement in this long derivation for the annual $\widetilde{\delta J}_y$ is in the forcing anomalies

$\delta\Omega$, which first appear in eqn. (S.2) as the total (i.e. un-decomposed) anomalies $\delta\Omega(\alpha)$

but by the end are in the form of the yearly anomalies $\delta\Omega_y$. With more effort, we can

continue to rearrange the "other terms" in the last line of eqn. (S.2) to get the equation

into the form:

$$\widetilde{\delta J}_y(t_a) \tag{S.3}$$

$$= \frac{\partial J}{\partial \Omega}(0)\delta\Omega_y(t_a) \quad + \frac{\partial J}{\partial \Omega}(1)\delta\Omega_y(t_a) \quad + ... + \frac{\partial J}{\partial \Omega}(11)\delta\Omega_y(t_a)$$

$$+ \frac{\partial J}{\partial \Omega}(12)\delta\Omega_y(t_a - 1) + \frac{\partial J}{\partial \Omega}(13)\delta\Omega_y(t_a - 1) + ... + \frac{\partial J}{\partial \Omega}(23)\delta\Omega_y(t_a - 1)$$

$$+\text{higher lag terms}$$

where the vector $\delta\Omega_y$ that enters into eqn. (S.3) is a **monthly** time-series and has in

the last twelve entries the same $\Omega_y(t_a)$ for the year of the reconstruction t_a, followed by

$\Omega_y(t_a - 1)$ of the prior year in the previous twelve entries, and so on. Now re-expressing eqn. (S.3) in the integral form and generalizing it to time t, we obtain:

$$\widetilde{\delta J}_y(t) = \int_{t_0}^{t} \frac{\partial J}{\partial \Omega}(\alpha - t)\delta \Omega_y(\alpha)d\alpha + \text{residuals} \qquad (S.4)$$

Finally, with the inclusion of the geographic integrals eqn. (S.4) becomes

$$\widetilde{\delta J}_y(t) \qquad\qquad (S.5)$$

$$= \int_{t_0}^{t} \int_{x_1} \int_{x_2} \frac{\partial J}{\partial \Omega}(x_1, x_2, \alpha - t)\delta \Omega_y(x_1, x_2, \alpha)dx_1 dx_2 d\alpha + \text{residuals}$$
$$\approx \int_{t_0}^{t} \int_{x_1} \int_{x_2} \frac{\partial J}{\partial \Omega}(x_1, x_2, \alpha - t)\delta \Omega_y(x_1, x_2, \alpha)dx_1 dx_2 d\alpha$$

Eqn. (S.5) is identical to eqn. (S.2) when the "residuals" are fully taken into account, and is a good approximation of eqn. (S.2) only if the "residuals" are small. To test if the "residual" in eqn. (S.5) are indeed small for the Bering transport anomaly reconstruction, we performed reconstructions of $\widetilde{\delta J}_{[y,c,res]}$, based on either the temporal decomposition of the full reconstructed $\widetilde{\delta J}$, eqn. (3), into annual, seasonal and monthly components, which we refer to as the "exact" method, or using eqn. (4), which we refer to as the "approx" method. Results are summarized in Fig. S3. In general, regardless of the method use, the reconstructed time-series $\widetilde{\delta J}_{approx}$ and $\widetilde{\delta J}_{exact}$ capture between 80–97% of the forward signal δJ_{fwd}. Up to 12-month lag, results of the temporal decomposition from the two methods are very similar. Beyond 12-month lags, some difference can be seen with the "exact" method capturing slightly less of the explained variance at seasonal and monthly time-scales (Fig. S3f,i).

The reformulation of the reconstruction following eqn. (S.5) and eqn. (4) now allows us to quantify the interannual, seasonal, and monthly transport anomalies directly from the components of the input forcing. See discussion in Section 3 for how this second "approx" method is used to investigate the direct relationship between extreme annual forcing wind stress anomalies and extrema in Bering Strait transport anomalies.
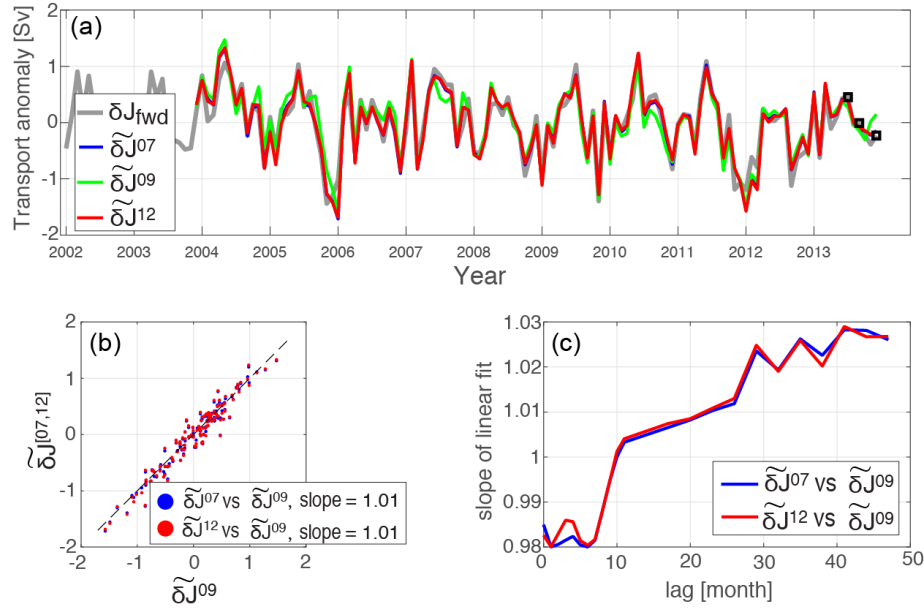
Figure S1. (a) Time-series of the transport anomaly from the forward model run (δJ_{fw}, thick gray) and the three different reconstruction ($\widetilde{\delta J}^{[07,09,12]}$) based on the sensitivity calculated from J of Jul/2013, Sep/2013, Dec/2013. The black squares are the values of $\delta J^{[07,09,12]}$. Reconstructions are summed over 24-month lags. (b) Scatter plots of reconstructed transport anomalies $\widetilde{\delta J}^{[07,12]}$ versus $\widetilde{\delta J}^{09}$, reconstructed using lags of up to 24 months. Values shown in the legend are the slope of the linear fit. (c) Slope of the linear fit using reconstructions summed up to lags ranging from 0–48months.
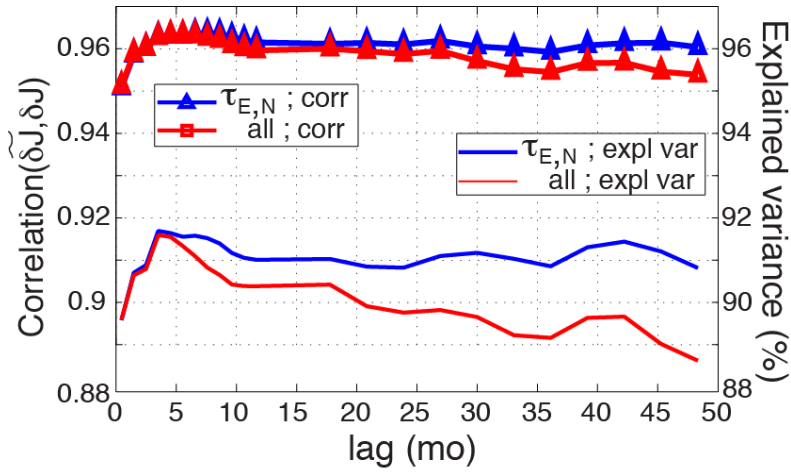
Figure S2.   Correlation and explained variance as a function of lags for reconstructed $\widetilde{\delta J}^{07}$, to be compared with Fig. 3b which was obtained with $\widetilde{\delta J}^{09}$. The behavior of the correlation and explained variance are the same regardless of the choice of $J^{[07,09,12]}$ used in the computation of the gradients and the subsequent reconstructed $\widetilde{\delta J}$.
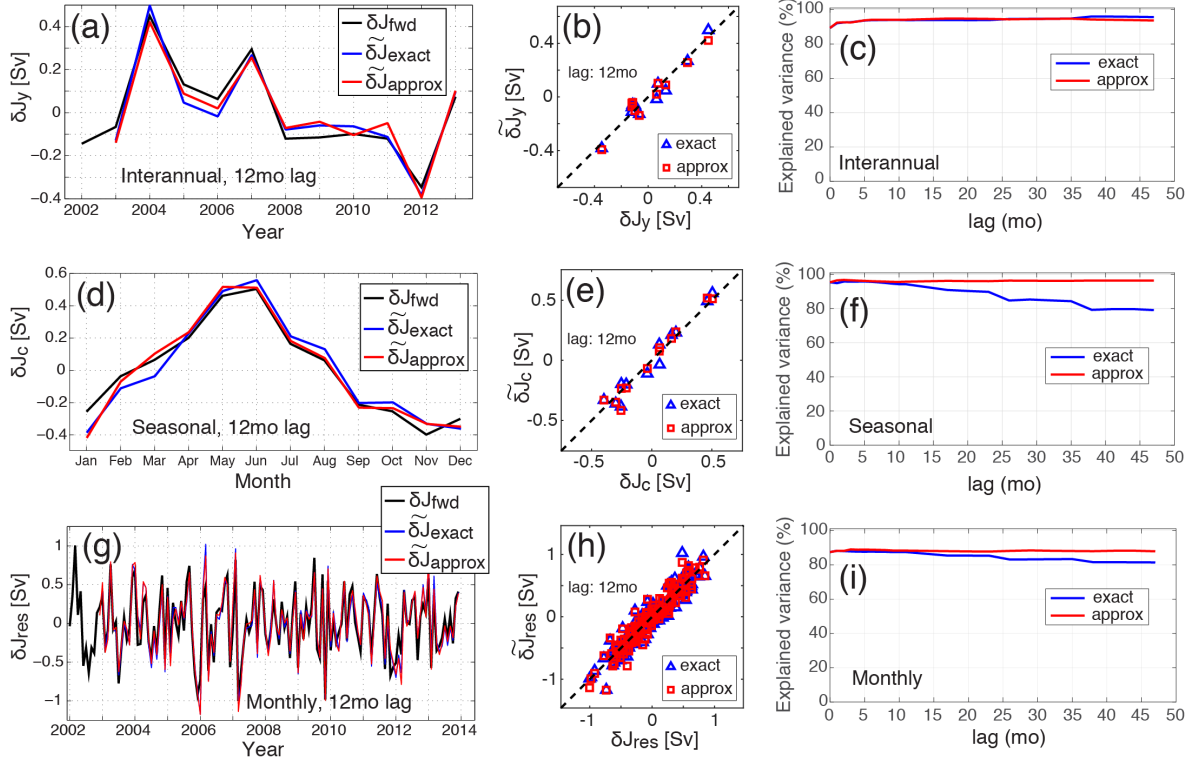
Figure S3.   Comparison of $\widetilde{\delta J}_{[y,c,res]}$ using methods "exact" versus "approx". The rows correspond to (a,b,c) interannual, (d,e,f) seasonal, and (g,h,i) monthly residual decompositions. The first column (a,d,g) compared time-series of $\widetilde{\delta J}$ using the two methods against the forward time series δJ_{fwd}. The second column (b,e,h) shows scatter plots of $\widetilde{\delta J}_{approx}$ versus $\widetilde{\delta J}_{exact}$ using lags of up to 12 months. The last column (c,f,i) shows the percentage of explained variance of each reconstructed $\widetilde{\delta J}$ relative to the forward time series δJ_{fwd} for all lags.